Anisotropic Mach Cone Aligned Mesh Adaptation for Low Boom Simulations

Chase P. Ashby*, Jeffrey A. Housman †, Jared Duensing ‡
NASA Ames Research Center, M/S 258-2, Moffett Field, CA 94035

An automated off-body Mach cone aligned structured curvilinear grid generation procedure is presented for near-field computational fluid dynamics simulations. This procedure combines output-based indicators and mesh redistribution to perform anisotropic mesh adaptation while maintaining Mach cone alignment. Automation is achieved through a novel direction-based adaptation indicator formulation. The adaptation procedure is demonstrated on the JAXA Wing Body geometry and X-59 C608 demonstrator model from the Second and Third AIAA Sonic Boom Prediction Workshops, respectively. It is demonstrated that anisotropic mesh adaptation may result in a greater than fifty percent reduction in resource usage required to achieve the same level of accuracy as uniform and user constructed Mach cone aligned grids for near-field pressure signatures, ground-level overpressure signatures, and loudness metrics.

I. Introduction

The evaluation of new low boom aircraft designs relies on accurate predictions of ground-level noise using high-fidelity numerical simulations. Commonly, these predictions rely on a two-step procedure. First, a near-field computational fluid dynamics (CFD) simulation models the three-dimensional, shock-dominated flow around the aircraft. Second, pressure traces are extracted from the CFD simulation to initialize a far-field propagation solver, which models the waveform as it travels from the extraction location to the ground. Minimization of the coupling errors requires a well-designed CFD mesh to capture important acoustic wave variations. This can be challenging given the shock-dominated, highly anisotropic nature of supersonic flow, leading to suboptimal performance for uniform grids in terms of mesh spacing, orientation, and size.

The goal of mesh adaptation is to generate an optimal mesh to minimize the errors present in the numerical solution, subject to computational resource constraints. Mesh adaptation has been successfully demonstrated to automatically improve sonic boom prediction accuracy while decreasing computational costs by reducing the number of cells required to achieve a desired accuracy level [1–6]. Fidkowski and Darmofal [7] provided an in-depth review of approaches for anisotropic mesh adaptation and output-based error indicators for CFD. More recently, Alauzet and Loseille [8] reviewed recent progress made in feature-based anisotropic mesh adaptation for complex flows involving shocks and boundary layers. Loseille applied anisotropic mesh adaptation to unstructured grids for the Second AIAA Sonic Boom Prediction Workshop (SBPW) comparing both Hessian and output-based indicators. Vanharen et al. [9] applied output-based anisotropic adaptation to the near-field cases of the Third AIAA SBPW. Park et al. [10] examined each step of an adaptation cycle: flow and adjoint solution, error estimation, metric construction, and mesh generation. Comparisons between several implementations for each of these individual adaptation steps were studied and later verified [11, 12]. Rangarajan et al. developed a continuous-mesh optimization approach to control the error in output functionals for high-order numerical methods [13]. Structured curvilinear overset grids systems with user-specified clustering on Mach cone aligned grids have successfully been used for sonic boom prediction [14–16]. However, to the authors' knowledge, no work has been published utilizing anisotropic mesh adaptation for this gridding methodology.

In this paper, we present an algorithm for automatically generating off-body Mach cone aligned structured curvilinear CFD grids using anisotropic mesh adaptation. This algorithm relies on a novel and versatile method for processing adaptation indicators on structured Mach cone aligned grids. Accuracy and efficiency are demonstrated on the JAXA Wing Body geometry and X-59 C608 demonstrator model from the Second and Third AIAA Sonic Boom Prediction Workshops, respectively. All adaptation results are benchmarked using an error indicator computed from extracted near-field pressure signatures.

---

*Computational Aerosciences Branch, chase.p.ashby@nasa.gov
†Computational Aerosciences Branch, AIAA Senior Member, jeffrey.a.housman@nasa.gov
‡Computational Aerosciences Branch, AIAA Member, jared.c.duensing@nasa.gov

II. Low Boom Simulation Procedure

A standard low boom simulation follows a two-step procedure which decomposed the sonic boom domain into overlapping near-field and far-field domains. Firstly, a compressible, inviscid or viscous, CFD simulation is performed in the near-field to a distance sufficiently far from the aircraft to avoid near-body azimuthal effects. The second step involves propagating extracted pressure signatures at a fixed radial distance from the aircraft along a ray path to the ground using a nonlinear Burgers' equation model. Recently, Housman et al. [17] introduced a three-step procedure which utilizes CFD for the near-field, space marching from the near-field to the mid-field, and acoustic propagation from the mid-field to the ground. This approach yields a computationally efficient prediction procedure while maintaining or enhancing accuracy.

We note that the terms near-field and mid-field describing the sonic boom domain decomposition are not to be confused with the overset terminology, near-body and off-body, which describe a partitioning of the CFD domain. The near-body includes both the aircraft surface and the volume of space a short distance away from the aircraft, while the off-body is defined to include the remaining volume of the CFD domain. Figure 1 shows an illustration of the sonic boom decomposition. By introducing an intermediate propagation step, the number of CFD grid points is reduced by at least 20-40 percent, which greatly mitigates the computational cost of the CFD simulation. This three-step low boom simulation approach has been verified for low boom aircraft designs [16].

In the near-field, three-dimensional steady-state Reynold's Averaged Navier-Stokes (RANS) equations governing compressible flow are solved using the Launch Ascent and Vehicle Aerodynamics (LAVA) framework [18]. The solution is then interpolated onto a set of fringe points to initialize LAVA's space marching solver that was developed by Housman et al. [17, 19]. The equations governing the evolution of the near-field supersonic flow to the mid-field are the three-dimensional steady-state Euler equations of gas dynamics. The definition of near-field to mid-field in this work is defined as the cylindrical region enclosing the aircraft with a starting radius of approximately 0.5 to 1.5 span lengths and extending to a radial distance of approximately 10 body lengths from the aircraft. Atmospheric effects, such as hydrostatic balance and thermal stratification, are negligible in this range.

The final step of the low boom simulation utilizes a far-field acoustic wave propagation code, sBOOM, which combines geometric acoustics with the augmented Burgers' equation in non-dimensional form [20, 21]. This solver is initialized from pressure waveforms extracted along a cylinder at a fixed radial distance from the aircraft. The far-field acoustic wave propagation results in ground-level sonic boom overpressure signatures and various loudness metrics. Among these loudness metrics are various weightings of Sound Exposure Level (A-, B-, and C-SEL) and a Perceived Loudness (PL) metric. These quantities are important for guiding low boom supersonic aircraft design and the establishment of flight planning tools.

III. Adaptation Methodology

The low boom simulations in this work consist of three coupled steps, errors resulting from the initial near-field CFD simulation will be accumulated within the space marching and far-field propagation procedures. We introduce a mesh adaptation procedure to control the discretization errors resulting from insufficient mesh resolution of the structured curvilinear Mach cone aligned off-body CFD grid. Figure 2 illustrates our adaptation cycle algorithm. To begin, an initial coarse Mach cone aligned off-body grid is automatically generated with uniform streamwise and circumferential spacing. This is combined with the near-body grid system using Chimera Grid Tools [22]. Overset connectivity is then performed using an implicit hole cutting approach to form the complete near-field structured curvilinear overset grid system. Next, the flow solver runs until the user-specified stopping criteria is satisfied. When output-based mesh adaptation is to be used, we require an adjoint linear system solve and corresponding embedding procedure to form our output-based error indicators. The final step in an adaptation cycle is to compute an error indicator and perform the off-body mesh adaptation. These steps are repeated for a user-specified number of cycles or until adaptation results in zero displacement. It is imperative to emphasize that overset connectivity must be performed at each adaptation cycle, since all interior off-body nodes are displaced. To greatly mitigate the associated computational cost, an internal implicit hole cutting connectivity code is employed within the LAVA framework.

A. Mach Cone Aligned Off-Body Mesh

Mach cone alignment is chosen since it reduces the artificial dissipation of the numerical method, hence requiring less grid points to achieve a specified level of error. A small perturbation μ_ϵ is applied to the mach angle $\mu = \sin^{-1}(1/M_\infty)$ to reduce the probability of the numerical flux being applied across a local sonic condition, which could potentially result in spurious oscillations. The inputs for the initial grid generation include: M_∞ the free-stream Mach number;

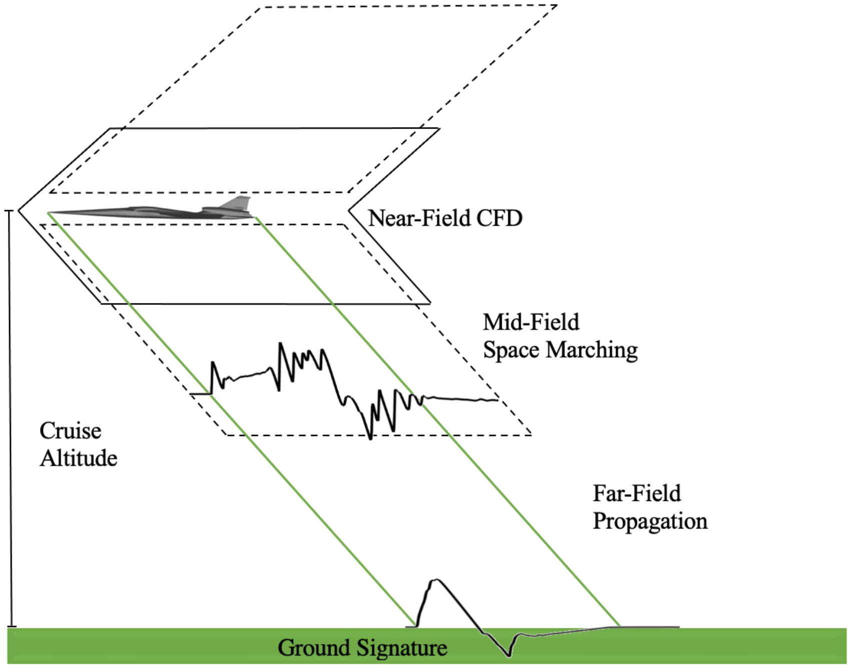

Fig. 1 Sonic boom domain decomposition.

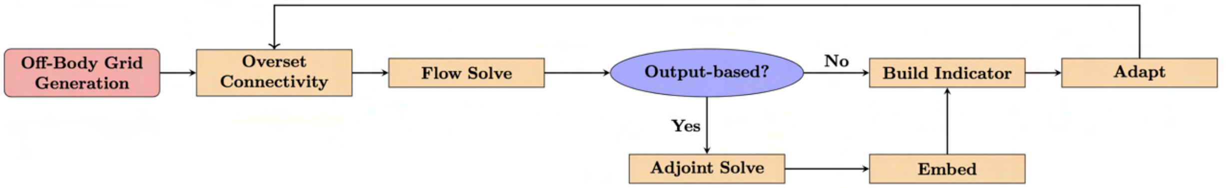

Fig. 2 Adaptation cycle flow chart.

$(\mathbf{x_0}, \boldsymbol{\theta_0})$ the starting axial and circumferential locations of the inner cylinder surface; $\mathbf{r}_0$ the starting point for stretching in the radial direction; $(\mathbf{x_{max}}, \mathbf{r_{max}}, \boldsymbol{\theta_{max}})$ the axial length, radial extent, and circumferential extent of the mesh; $\mathbf{N}_\mathrm{s}$ and $\mathbf{N}_\theta$ the number of points in the streamwise axial and circumferential directions; $\mathbf{N}_\mathrm{r}$ the minimum number of points in the radial direction; $\mathbf{SR}$ and $\mathbf{AR}_\mathrm{max}$ the stretching ratio and maximum aspect ratio in the radial direction.

The initial grid generation procedure begins by constructing a line segment. Circumferential spacing of length $\Delta\boldsymbol{\theta} = (\boldsymbol{\theta}_\mathrm{max} - \boldsymbol{\theta}_0)/(\mathbf{N}_{\boldsymbol{\theta}} - 1)$ is used to discretize the line to an extent $\mathbf{r}_0$. Then the user provided stretching ratio $\mathbf{SR}$ is applied until the maximum aspect ratio or $\mathbf{r}_\mathrm{max}$ is reached, increasing $\mathbf{N}_\mathrm{r}$ as needed. The line is rotated to the perturbed Mach cone angle $\mu + \mu_\varepsilon$ and is used to produce a $\xi - \zeta$ symmetry plane by discretizing the streamwise direction with uniform spacing $\Delta\mathbf{s} = (\mathbf{x}_\mathrm{max} - \mathbf{x}_0)/(\mathbf{N}_\mathrm{s} - 1)$. Next, the plane is revolved to $\boldsymbol{\theta}_\mathrm{max}$ using uniform circumferential spacing $\Delta\boldsymbol{\theta}$. Finally, the three-dimensional Mach cone aligned grid is translated and rotated to its origin $(\mathbf{x_0}, \boldsymbol{\theta}_0)$. An example of a resulting automatically generated off-body grid is shown in Figure 3.

B. Mesh Redistribution

Adaptation is achieved through an r-refinement algorithm, which fixes the number of grid points and redistributes them to coarsen or refine certain regions of the grid. This adaptation approach can be viewed as a method for generating an optimal off-body grid for a given number of degrees of freedom, and for the current application a fixed mesh

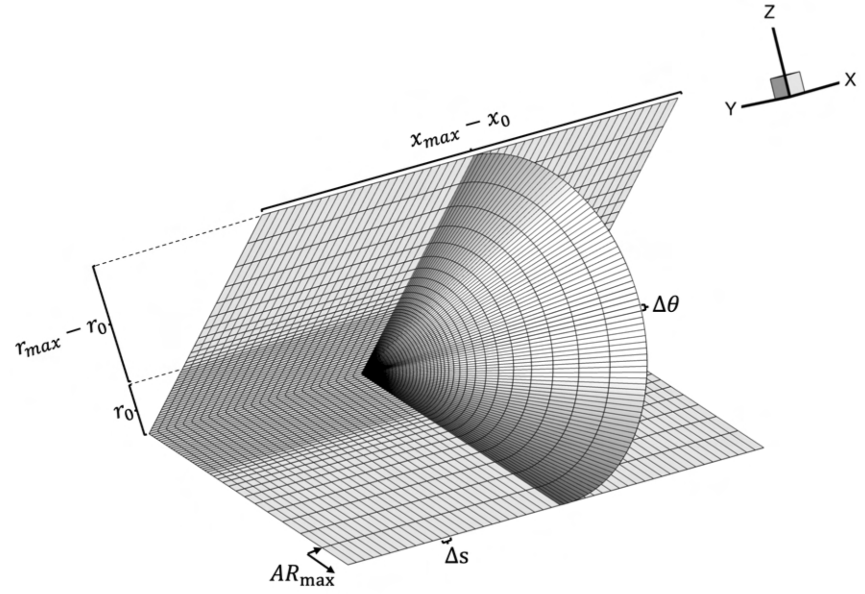

Fig. 3 Symmetry plane and streamwise slice of a Mach cone aligned off-body mesh automatically generated from user-specified parameters.

orientation. Governing the mesh redistribution is a one-dimensional error equidistribution principle of the form

$$w_i \Delta s_i = C \tag{1}$$

for $i = 1, \ldots, N$. Here, N is the number of grid points along the one-dimensional curvilinear coordinate line, w_i is a positive weighting function, $\Delta s_i = s_{i+1} - s_i$ is the length of the i^{th} interval, and C is an arbitrary constant. The weighting function is defined as

$$w_i = 1 + A f_i \tag{2}$$

where f_i is the error indicator which drives the redistribution and A is a user-specified clustering constant. By requiring $0 \le f_i \le 1$, the minimum and maximum grid spacing satisfy,

$$\Delta s_{\text{min}} = \frac{s_{\text{max}}}{(1 + A) \sum_i w_i^{-1}} \tag{3}$$

and

$$\Delta s_{\text{max}} = \frac{s_{\text{max}}}{\sum_i w_i^{-1}} \tag{4}$$

where s_{max} is the length of the one-dimensional adaptation domain. The clustering constant A immediately follows from these relations

$$A = \frac{\Delta s_{\text{max}}}{\Delta s_{\text{min}}} - 1 \tag{5}$$

The choice of the minimum and maximum allowable grid spacing ratio is user-specified; however, methods for determining automatically the appropriate spacing are currently under investigation. One such approach is to define Δs^0_{max} and Δs^0_{min} to be the initial coarse grid maximum and minimum spacing. Then, if we introduce user-specified coarsening and refinement factors, c_{f} and r_{f}, target spacing can be defined as

$$\Delta s_{\min} = \frac{1}{r_{\mathrm{f}}} \Delta s^{0}_{\min} \tag{6}$$

$$\Delta s_{\max} = c_{\mathrm{f}} \Delta s^{0}_{\max} \tag{7}$$

The clustering constant becomes,

$$A = c_{\mathrm{f}} r_{\mathrm{f}} \frac{\Delta s^{0}_{\max}}{\Delta s^{0}_{\min}} - 1 \tag{8}$$

which places restrictions on the amount of local coarsening and refinement.

Following the equidistribution principle in equation (1), we fix our boundary points and want to find new interior grid point locations $\mathbf{s}$, such that their associated error weights satisfy

$$\Delta \mathbf{s}_i w_i - \Delta \mathbf{s}_{i-1} w_{i-1} = 0 \tag{9}$$

for $i = 2, \ldots, N-1$. This forms a nonlinear system of equations $\mathbf{F}(\mathbf{s}) = \mathbf{0}$ with

$$F_i = w_{i-1} s_{i-1} - (w_{i-1} + w_i) s_i + w_i s_{i+1} \tag{10}$$

where F_i is the i^{th} element of $\mathbf{F}(\mathbf{s})$. These equations are iteratively solved using Newton's method with an update step

$$\mathbf{s}^{n+1} = \mathbf{s}^{n} + \alpha \Delta \mathbf{s}^{n} \tag{11}$$

where the step size, $\alpha > 0$, is determined via a backtracking line search with stopping criteria specified by the Armijo-Goldstein inequality [23]. Further details discussing the selection of alternative weighting functions and constants can be found in [24, 25].

IV. Error Indicators

Direction-based redistribution requires indicators which accurately capture the error as it varies in the specified adaptation direction. The formulation of such indicators begins with the computation of canonical error indicators for CFD volume grids. A novel procedure is then used to transform these CFD volume grid indicators into direction-based indicators. For completeness, we will first introduce the feature-based and output-based error indicators used within this work.

A. Output-based Indicators

We begin by deriving the method of discrete adjoint-weighted residuals for finite-volume and finite-difference discretizations for near-field CFD simulations, following the work of [3, 26, 27]. Consider an open bounded domain $\Omega \subset \mathbb{R}^d$, $1 \le d \le 3$. We denote the output quantity of interest as $J(\mathbf{Q})$, where $\mathbf{Q}$ is the analytic solution to a set of model equations,

$$\mathbf{R}(\mathbf{Q}) = \mathbf{0} \text{ in } \Omega \tag{12}$$

For this work we apply the RANS equations in strong conservative form where Ω is the near-field CFD domain. Suppose Ω has been discretized to form a working mesh Ω_{H} with characteristic cell-size H and N vertices. The flow equations are then discretized and form a nonlinear discrete system of partial differential equations,

$$\mathbf{R}_{\mathrm{H}}(\mathbf{Q}_{\mathrm{H}}) = \mathbf{0} \tag{13}$$

where $\mathbf{Q}_{\mathrm{H}} = [\mathbf{Q}_1, \ldots, \mathbf{Q}_N]^T$, $\mathbf{Q}_i \in \mathbb{R}^M$, and $\mathbf{R}_{\mathrm{H}} \in \mathbb{R}^{M \cdot N}$. If J was an integral operator, then J_{H} represents the quadrature rule used to compute J on Ω_{H}. Our primary goal in this section is to derive an error estimate for the functional discretization error,

$$\varepsilon = |J(\mathbf{Q}) - J_{\mathrm{H}}(\mathbf{Q}_{\mathrm{H}})| \tag{14}$$

Let Ω_{h} be the embedded uniformly refined mesh with characteristic cell-size satisfying $h = H/r_{\mathrm{f}}$ where $r_{\mathrm{f}} \in \mathbb{Z}_{+}$ is the refinement factor. The Richardson extrapolation method follows the assumption that as long as the solution is within the asymptotic range, the functional discretization error satisfies the relations

$$J_{\mathrm{H}}(\mathbf{Q}_{\mathrm{H}}) - J(\mathbf{Q}) = g_{\mathrm{p}} H^{p} + O(H^{p+1}) \tag{15}$$

and

$$J_{\mathrm{h}}(\mathbf{Q}_{\mathrm{h}}) - J(\mathbf{Q}) = g_{\mathrm{p}} h^{p} + O(h^{p+1}) \tag{16}$$

where g_{p} depends only on the formal order of accuracy p. Solving for g_{p} and substituting gives a relation between the coarse and fine grid functional discretization error

$$J(\mathbf{Q}) - J_{\mathrm{H}}(\mathbf{Q}_{\mathrm{H}}) = \frac{r_{\mathrm{f}}^{p}}{r_{\mathrm{f}}^{p} - 1}\left(J_{\mathrm{h}}(\mathbf{Q}_{\mathrm{h}}) - J_{\mathrm{H}}(\mathbf{Q}_{\mathrm{H}})\right) + O(h^{p+1}) \tag{17}$$

Equation (17) replaces the need for the analytic solution, however, still requires the computation of the fine grid solution $\mathbf{Q}_{\mathrm{h}}$. Obtaining this solution can be prohibitively expensive. In order to adhere to potential cost constraints, it is advantageous to seek an approximation to $J_{\mathrm{h}}(\mathbf{Q}_{\mathrm{h}})$ using discrete adjoint theory. The discrete adjoint (or dual) problem is a linear system of equations of the form

$$\left[\frac{\partial \mathbf{R}_{\mathrm{H}}}{\partial \mathbf{Q}_{\mathrm{H}}}\bigg|_{\mathbf{Q}_{\mathrm{H}}}\right]^{T} \boldsymbol{\psi}_{\mathrm{H}} = \left[\frac{\partial J_{\mathrm{H}}}{\partial \mathbf{Q}_{\mathrm{H}}}\bigg|_{\mathbf{Q}_{\mathrm{H}}}\right]^{T} \tag{18}$$

Linearizing the embedded grid residual and output functional about a perturbed state gives

$$\mathbf{0} = \mathbf{R}_{\mathrm{h}}(\mathbf{Q}_{\mathrm{h}}) \approx \mathbf{R}_{\mathrm{h}}(\mathbf{Q}_{\mathrm{h}}^{\mathrm{H}}) + \frac{\partial \mathbf{R}_{\mathrm{h}}(\mathbf{Q}_{\mathrm{h}}^{\mathrm{H}})}{\partial \mathbf{Q}_{\mathrm{h}}}\left(\mathbf{Q}_{\mathrm{h}} - \mathbf{Q}_{\mathrm{h}}^{\mathrm{H}}\right) \tag{19}$$

and

$$J_{\mathrm{h}}(\mathbf{Q}_{\mathrm{h}}) \approx J_{\mathrm{h}}(\mathbf{Q}_{\mathrm{h}}^{\mathrm{H}}) + \frac{\partial J_{\mathrm{h}}(\mathbf{Q}_{\mathrm{h}}^{\mathrm{H}})}{\partial \mathbf{Q}_{\mathrm{h}}}\left(\mathbf{Q}_{\mathrm{h}} - \mathbf{Q}_{\mathrm{h}}^{\mathrm{H}}\right) \tag{20}$$

where $\mathbf{Q}_{\mathrm{h}}^{\mathrm{H}} = \mathbf{P}\mathbf{Q}_{\mathrm{H}}$ is the prolonged working mesh solution and $\mathbf{P}$ is the prolongation operator. Combining (19) and (20),

$$J_{\mathrm{h}}(\mathbf{Q}_{\mathrm{h}}) - J_{\mathrm{h}}(\mathbf{Q}_{\mathrm{h}}^{\mathrm{H}}) \approx -\frac{\partial J_{\mathrm{h}}(\mathbf{Q}_{\mathrm{h}}^{\mathrm{H}})}{\partial \mathbf{Q}_{\mathrm{h}}}\left(\frac{\partial \mathbf{R}_{\mathrm{h}}(\mathbf{Q}_{\mathrm{h}}^{\mathrm{H}})}{\partial \mathbf{Q}_{\mathrm{h}}}\right)^{-1} \mathbf{R}_{\mathrm{h}}(\mathbf{Q}_{\mathrm{h}}^{\mathrm{H}}) = -(\boldsymbol{\psi}_{\mathrm{h}})^{T} \mathbf{R}_{\mathrm{h}}(\mathbf{Q}_{\mathrm{h}}^{\mathrm{H}}) \tag{21}$$

Adding and subtracting a prolonged adjoint solution gives,

$$J_{\mathrm{h}}(\mathbf{Q}_{\mathrm{h}}) - J_{\mathrm{h}}(\mathbf{Q}_{\mathrm{h}}^{\mathrm{H}}) \approx -\left(\boldsymbol{\psi}_{\mathrm{h}}^{\mathrm{H}}\right)^{T} \mathbf{R}_{\mathrm{h}}(\mathbf{Q}_{\mathrm{h}}^{\mathrm{H}}) - \left(\boldsymbol{\psi}_{\mathrm{h}} - \boldsymbol{\psi}_{\mathrm{h}}^{\mathrm{H}}\right)^{T} \mathbf{R}_{\mathrm{h}}(\mathbf{Q}_{\mathrm{h}}^{\mathrm{H}}) \tag{22}$$

The first term on the right-hand side is a computable correction to the discrete output functional calculation, while the second term relies on a fine grid adjoint solution and approximates the remaining error after correction. To avoid solving the adjoint linear system on the embedded mesh, we apply low- and high-order prolongation operators to the working mesh primal and adjoint solutions, $\mathbf{Q}_{\mathrm{h}}^{\mathrm{LO}} = \mathbf{P}_{\mathrm{LO}}\mathbf{Q}_{\mathrm{H}}$, $\boldsymbol{\psi}_{\mathrm{h}}^{\mathrm{LO}} = \mathbf{P}_{\mathrm{LO}}\boldsymbol{\psi}_{\mathrm{H}}$, and $\boldsymbol{\psi}_{\mathrm{h}}^{\mathrm{HI}} = \mathbf{P}_{\mathrm{HI}}\boldsymbol{\psi}_{\mathrm{H}}$. Replacing $\boldsymbol{\psi}_{\mathrm{h}}$, $\boldsymbol{\psi}_{\mathrm{h}}^{\mathrm{H}}$, and $\mathbf{Q}_{\mathrm{h}}^{\mathrm{H}}$ in (22) gives

$$J_{\mathrm{h}}(\mathbf{Q}_{\mathrm{h}}) - J_{\mathrm{h}}(\mathbf{Q}_{\mathrm{h}}^{\mathrm{LO}}) \approx -\left(\boldsymbol{\psi}_{\mathrm{h}}^{\mathrm{LO}}\right)^{T} \mathbf{R}_{\mathrm{h}}(\mathbf{Q}_{\mathrm{h}}^{\mathrm{LO}}) - (\boldsymbol{\psi}_{\mathrm{h}}^{\mathrm{HI}} - \boldsymbol{\psi}_{\mathrm{h}}^{\mathrm{LO}})^{T} \mathbf{R}_{\mathrm{h}}(\mathbf{Q}_{\mathrm{h}}^{\mathrm{LO}}) \tag{23}$$

Substituting this approximation into(17),

$$J(\mathbf{Q}) - J_{\mathrm{H}}(\mathbf{Q}_{\mathrm{H}}) \approx \frac{r_{\mathrm{f}}^{p}}{r_{\mathrm{f}}^{p}-1}\left(J_{\mathrm{h}}(\mathbf{Q}_{\mathrm{h}}^{\mathrm{LO}}) - J_{\mathrm{H}}(\mathbf{Q}_{\mathrm{H}})\right) - \frac{r_{\mathrm{f}}^{p}}{r_{\mathrm{f}}^{p}-1}\left[\left(\boldsymbol{\psi}_{\mathrm{h}}^{\mathrm{LO}}\right)^{T}\mathbf{R}_{\mathrm{h}}(\mathbf{Q}_{\mathrm{h}}^{\mathrm{LO}}) + (\boldsymbol{\psi}_{\mathrm{h}}^{\mathrm{HI}} - \boldsymbol{\psi}_{\mathrm{h}}^{\mathrm{LO}})^{T}\mathbf{R}_{\mathrm{h}}(\mathbf{Q}_{\mathrm{h}}^{\mathrm{LO}})\right] \tag{24}$$

The output-based error estimate on the embedded off-body grid is defined to be the error in the computable correction,

$$e_{\mathrm{h}} = (\boldsymbol{\psi}_{\mathrm{h}}^{\mathrm{HI}} - \boldsymbol{\psi}_{\mathrm{h}}^{\mathrm{LO}})^{T}\mathbf{R}_{\mathrm{h}}(\mathbf{Q}_{\mathrm{h}}^{\mathrm{LO}}) \tag{25}$$

A full-weighting restriction operator is applied to e_{h} to produce the error indicator e_0 on the working off-body mesh.

To ensure robustness and reduced computational resource usage for complex supersonic cases, we do not form the exact discrete adjoint linear system. Instead, an approximate discrete adjoint linear system is constructed. The left-hand side approximate residual Jacobian is formed using a nearest-neighbor perturbation. An ILU preconditioner with low fill level is formed from the approximate Jacobian and the preconditioned approximate linear system is solved using restarted GMRES. These approximations result in a fast adjoint solve time, with computational costs not exceeding more than 10% of the cost incurred by the associated second-order nonlinear primal solver. Assessments of a second-order adjoint solver demonstrated no significant advantages over the low-order adjoint solver for mesh redistribution applications.

For our three-step sonic boom prediction procedure, we are concerned with minimizing the discretization error introduced to the space marching domain resulting from insufficient off-body grid resolution. The initial layers of the space marching domain are initialized from the CFD solution through an explicit elliptic hole cutting algorithm, which generates fringe points used for interpolation [19]. The user provides an origin and minimal radii defining an elliptic surface to encapsulate the model geometry and avoid the thin boundary layer to ensure the Euler and RANS equations match in the overlapping region of the CFD and space marching domain. An ellipse is chosen to allow for a tight fit of the geometry. Figure 4 shows the a priori user generated elliptic surface defining the near-field and space marching interface location, along with the resulting fringe points plotted with two space marching surfaces for context. Since the space marching solution only depends on the CFD solution at these fringe point locations, our output quantity of interest is defined as the discrete functional

$$J(\mathbf{Q}) := \sum_{i=1}^{N_{\mathrm{fringe}}} \left(\frac{\Delta p_i}{p_\infty}\right)^2 \tag{26}$$

where N_{fringe} is the number of fringe points.

B. Feature-based Indicator

Here we present a simple error indicator based on the work of Buning and Pulliam [28]. The one-dimensional undivided second-difference of a flow quantity q is computed at point i

$$s_i = q_{i+1} - 2q_i + q_{i-1} \tag{27}$$

This is a computational coordinate biased proxy for q at grid point i and is proportional to the remaining error term of the linear interpolation of q from neighboring points on a two times coarser grid level. Common examples of q for supersonic flow include Mach number and pressure disturbance. For a given computational coordinate direction, non-blanked points are computed

$$e(\xi_j, \eta_k, \zeta_l) = \max_{i=j,k,l} \frac{|q_{i+1} - 2q_i + q_{i-1}|}{q_{\mathrm{ref}}} \tag{28}$$

where q_{ref} is a reference quantity used to normalize the indicator.

C. Direction-Based Indicator Formulation

To ensure direction-based redistribution produces high-quality volume grids, we apply a novel procedure to the aforementioned error indicators. Let $e_0 = e_0(\xi, \eta, \zeta)$ be an initial error indicator computed on the Mach cone aligned off-body grid where ξ, η, and ζ are the streamwise, circumferential, and radial computational grid axes respectively.

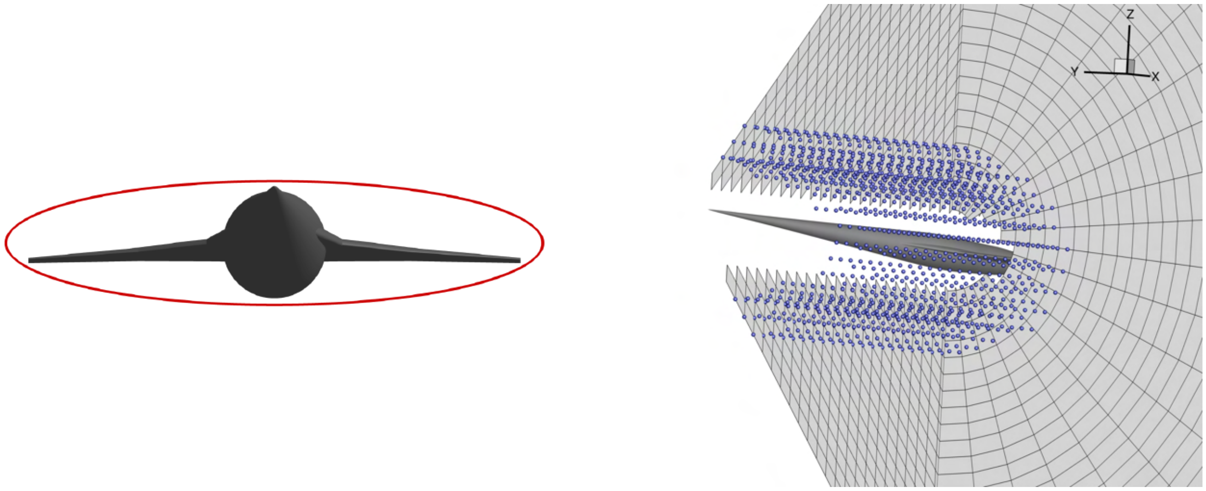

Fig. 4 Elliptic hole cutting surface defining the near-field CFD and space marching interface location shown on the (left), and the resulting fringe points plotted with two slices of the space marching grid shown on the right(right).

Since supersonic flow information travels in a common time-like direction, we form a new indicator from e_0 such that the adaptation will generate locally refined spacing along the time-like direction while maintaining required mesh alignment and smoothness. Without loss of generality, we proceed by outlining the procedure for forming a streamwise adaptation indicator. An initial streamwise adaptation indicator g is defined

$$g(\xi) = \max_{\eta} |e_0(\xi, \eta, \zeta^*)| \tag{29}$$

where ζ^* is the cylindrical surface with minimum radial distance from the aircraft that is not blanked by the near-body grid system. This ensures the capturing of the errors in the circumferential direction at each streamwise location on the fixed radial surface. An elliptic smoothing algorithm is applied to the indicator,

$$g_i^{\mathrm{s}} = \frac{g_{i-1} + 4g_i + g_{i+1}}{6} \tag{30}$$

where $g_i = g(\xi_i)$ [29]. Applying this algorithm for a low number of iterations reduces numerical noise and sets values in the blanked points with reasonable approximations for adaptation. Let $\bar{g}$ be the average of the smooth streamwise indicator. Since $g^{\mathrm{s}} \geq 0$ and we require $g^{\mathrm{s}} \in [0, 1]$ in order to specify the clustering constant A in equation (2), we define the mapping

$$f(\xi, \eta; \zeta^*) = \tanh(\beta\, g^{\mathrm{s}}(\xi)) \in [0, 1) \tag{31}$$

where $\beta = \tanh^{-1}(0.8)/(C\,\bar{g})$ and $C \geq 1$ is a threshold constant ensuring the targeting of statistically significant regions of the error indicator. Once the surface indicator $f(\xi, \eta; \zeta^*)$ is defined, we interpolate its values onto the rest of the grid using a normalized distance metric

$$\tau = \frac{x - r\sqrt{M_\infty^2 - 1}}{L_{\mathrm{body}}} \tag{32}$$

where r is the radial distance from the aircraft centerline and L_{body} is the aircraft body length. This metric is detailed in Figure 6.

An example of the one-dimensional formulation procedure is shown in Figure 5 for an axisymmetric body geometry. Twenty elliptic smoothing iterations are applied to the noisy initial indicator. Figure 5b shows thresholds corresponding to constants $C = 1$ and $C = 4$ where the average is computed from the smoothed indicator. The final one-dimensional indicators corresponding to the unique mappings defined by these threshold constants are shown in 5c and 5d, respectively. Choosing $C = 1$ results in equal weighting of the features present in the initial smooth signature. In contrast, since the threshold defined by $C = 4$ is greater than all but the most significant feature, the relative magnitudes of the smooth indicator features are better preserved. This adaptation procedure is generalizable to other computational space directions, including the ability to handle multiple off-body blocks sharing block-to-block boundaries.

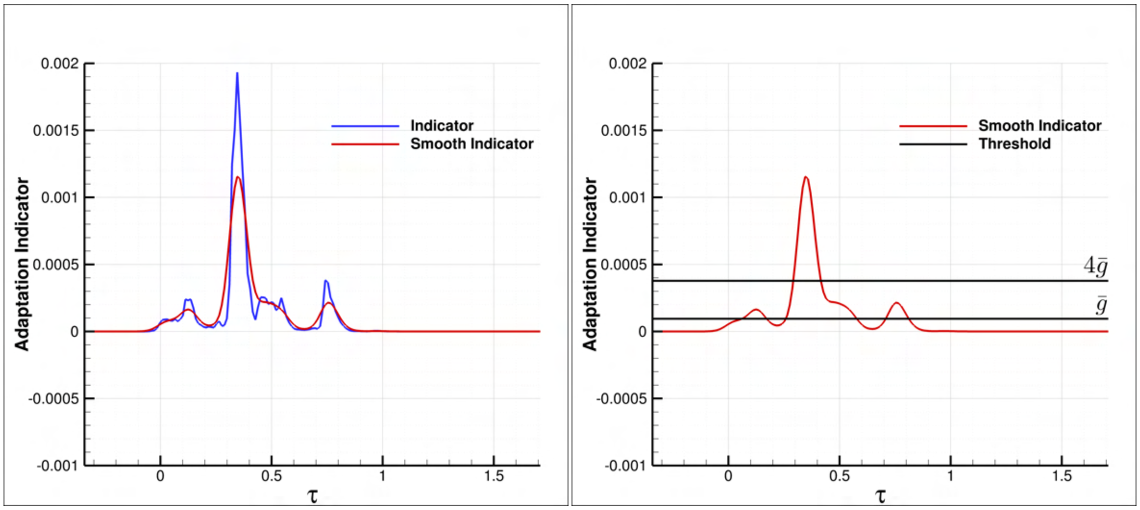

(a) Initial adaptation indicator g (blue) and elliptically smoothed indicator g^s (red).

(b) Smoothed adaptation indicator thresholds corresponding to threshold constants $C = 1$ and $C = 4$.

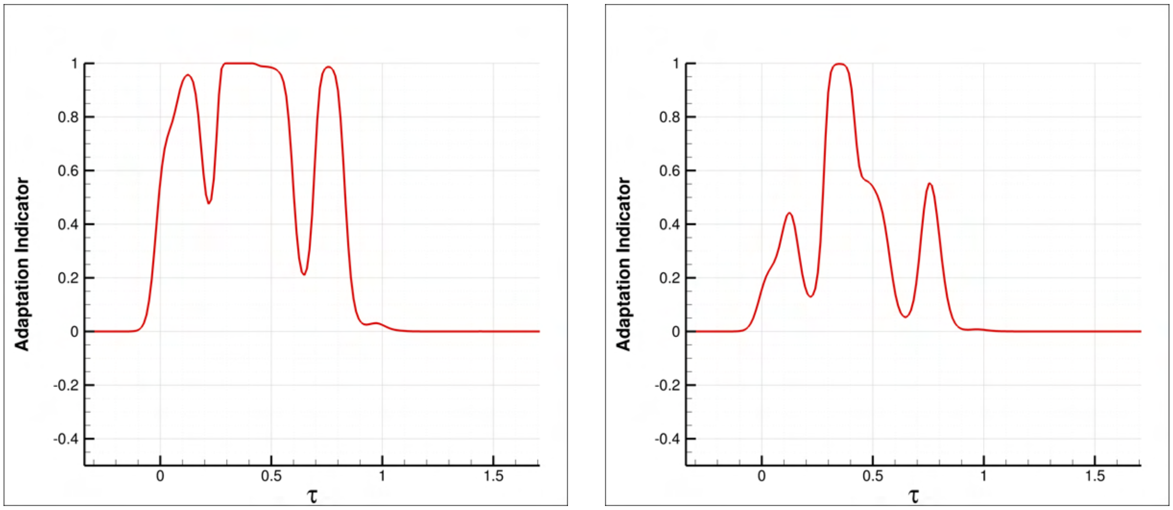

(c) Final indicator using $\bar{g}$ threshold.

(d) Final indicator using $4\,\bar{g}$ threshold.

Fig. 5 Streamwise adaptation indicator formulation using 20 elliptic smoothing iterations and two different user-specified mapping thresholds

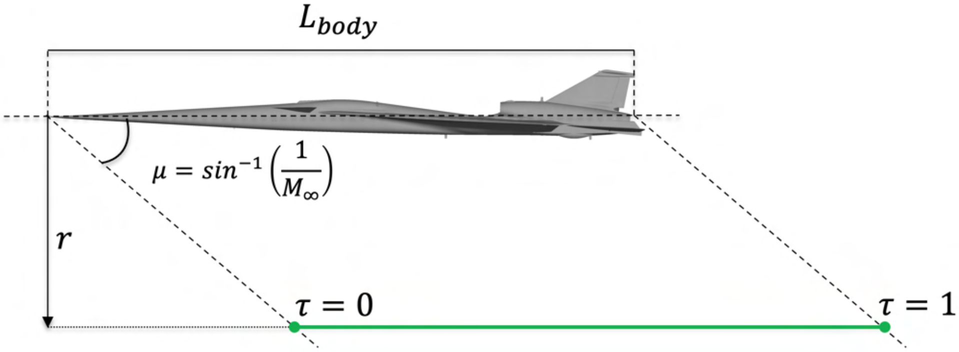

Fig. 6 Normalized distance metric.

V. Results

The automated off-body Mach cone aligned mesh generation procedure described above is used to propagate several near-field CFD solutions for a low boom aircraft geometry from the Second and Third AIAA Sonic Boom Prediction Workshops. By fixing the near-body grid system, we demonstrate the cost and accuracy benefits of applying our anisotropic mesh adaptation algorithm to the automated off-body grids using feature-based and output-based indicators. The feature-based adaptation indicator in (28) is defined with Mach number as the flow quantity q. We begin by presenting a method for benchmarking the adaptation procedure.

A. Adaptation Benchmark

A conservative performance benchmark is constructed from an approximation to the exact error sensor. For a fixed space marching grid resolution, coarse and fine space marching grid solutions are extracted at some fixed radial distance r from the aircraft centerline and azimuthal angle ϕ. The pointwise error is computed between these two extracted waveforms

$$\varepsilon_i = \left| \frac{p_{\mathrm{h},i} - p_{\mathrm{H},i}}{p_\infty} \right| \tag{33}$$

where p_{H} and p_{h} are the coarse and fine grid pressure along the extracted line probe, respectively. Since all information travels along characteristic surfaces, we interpolate the pointwise difference back onto the off-body CFD grid using the normalized distance metric in equation (32). This pointwise error approximation is then used to form an error indicator for adaptation using the same procedure as described in Section IV. This process is repeated for each radial extraction distance and azimuthal angle studied. Figure 7 shows an indicator formed on the ζ^*-surface for the JAXA Wing Body (JWB) geometry.

B. JAXA Wing Body

The JWB geometry was a part of the Second AIAA Sonic Boom Prediction Workshop and is shown in Figure 8. This aircraft is a L_{body} = 38.7 meter long wing-body configuration flying at Mach 1.6 at an angle of attack of 2.3 degrees and cruise altitude of 15.76 kilometers. These conditions result in a flight Reynolds number of 5.7 million per meter. A CFD mesh refinement study was performed during the workshop, and the coarse grid system, which was deemed sufficient based on that study, is used for all reported results.

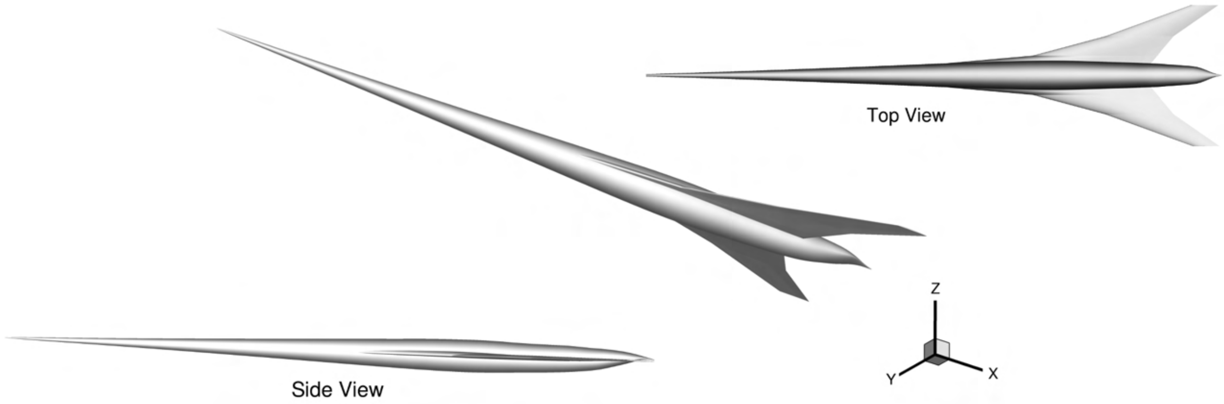

Fig. 8 JAXA Wing Body geometry from then Second AIAA Sonic Boom Prediction Workshop.

The automatically generated off-body grid has a streamwise domain length of 1.47 L_{body} and circumferential extent of 180° discretized with uniform spacing into N_{s} = 201 streamwise and N_θ = 181 circumferential points, respectively. Finally, a stretching ratio of SR = 1.05 and maximum aspect ratio of $AR_{\max}$ = 20 are applied in the radial direction, with a domain extent $r_{\max}$ = 0.47 L_{body} discretized into N_{r} = 257 points. The coarse grid has 12,713,397 total nodes, of which 6,325,532 nodes comprise the off-body grid. Since only streamwise adaptation is performed, a fine grid is constructed by uniformly refining the off-body grid in the streamwise direction with a refinement factor r_{f} = 4. The fine off-body grid

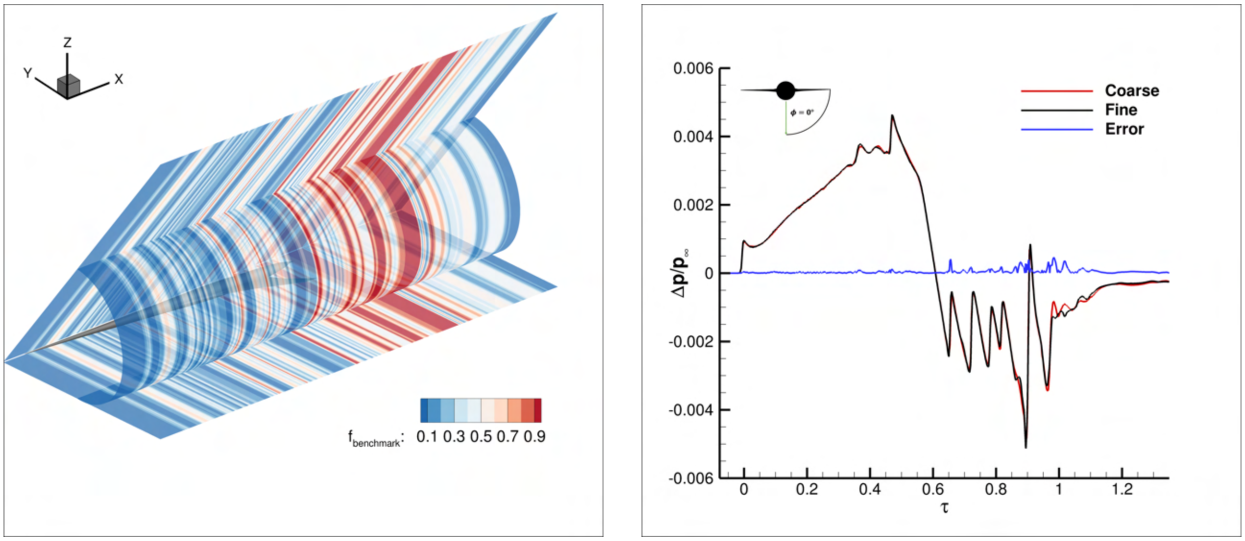

(a) **(b)**

Fig. 7 (a) Benchmark error indicator formed from the pointwise error between on-track coarse and fine near-field pressures signatures at a radial distance $r/L_{\mathbf{body}} = 3$. (b) Near-field signatures and pointwise error.

has 25,226,694 nodes, resulting in a total grid system node count of 32,057,559. Adaptation is performed on the coarse mesh using feature-based, output-based, and benchmark adaptation indicators. The feature-based adaptation indicator is defined using Mach number for the flow quantity in 28. All adaptation parameters are automatically set according to our determined best practices to $\beta = \tanh^{-1}(0.8)/4\,\bar{g}$ and $A = 10$. Only one adaptation cycle has been performed for each indicator, since it was found that multiple adaptation cycles do not result in additional improvements over a single cycle. The RANS equations are solved using a third-order upwind flux with a Koren limiter and SA-RC-QCR2000 turbulence model. The final adapted coarse grids are shown in Figure 9 colored by pressure disturbance $\Delta p/p_\infty$.

The adapted CFD grid solutions are space marched from the near-field to the mid-field using LAVA's high-fidelity space marching solver. We apply the best practices established for the JWB geometry by Housman et al. [17]. The space marching grid domain extends five body lengths and is discretized into 64,111,467 nodes. The three-dimensional Euler equations are discretized using a fourth-order Hybrid Weighted Compact Nonlinear scheme with fifth-order WENO interpolation in the non-space marching direction and second-order backward differentiation is used in the space marching direction. The two-dimensional nonlinear system is solved at each space marching station using an alternating line Jacobi relaxation. Line probes are extracted from the converged space marching solution at radial distances $r/L_{\text{body}} = 1$ and $r/L_{\text{body}} = 3$.

1. Near-field Signature Results

Figures 11 and 12 show on-track and off-track pressure signatures extracted at $r/L_{\text{body}} = 1$. The feature-based and output-based adapted grid results compare favorably. From Figure 11, we observe that the output-based adapted grid matches the fine grid signature better than both the Mach and benchmark adapted signatures. In Figure 12, both the output-based and benchmark adapted signatures accurately capture the strong shock formed at $\tau = 0.95$. In contrast, the Mach adapted solution matches the fine grid results in the pressure trough just after the strong shock. Figures 13 and 14 show both on-track and off-track pressure signatures extracted at $r/L_{\text{body}} = 3$. The Mach adapted and output-based adapted signatures agree at the strong shock locations, however, the output-based performs much better at the weak shocks upstream for $0.3 \le \tau \le 0.6$. From the symmetry plane slices in Figure 9, we see that the output-based adapted grid solution is resolving flow features from at the leading edge of the wings to the aft portion of the aircraft, while the Mach adapted solution captures a significant terminating shock right after the fuselage. This may be causing the differences we are seeing in the near-field extracted signatures.

Figure 9a shows grid refinement far downstream, which automatically prompts under-resolution in several shock locations for the benchmark adapted solution. Consequently, the benchmark adapted and fine grid pressure signatures show large disagreements at both strong and weak shocks. Further disagreement between near-field to mid-field

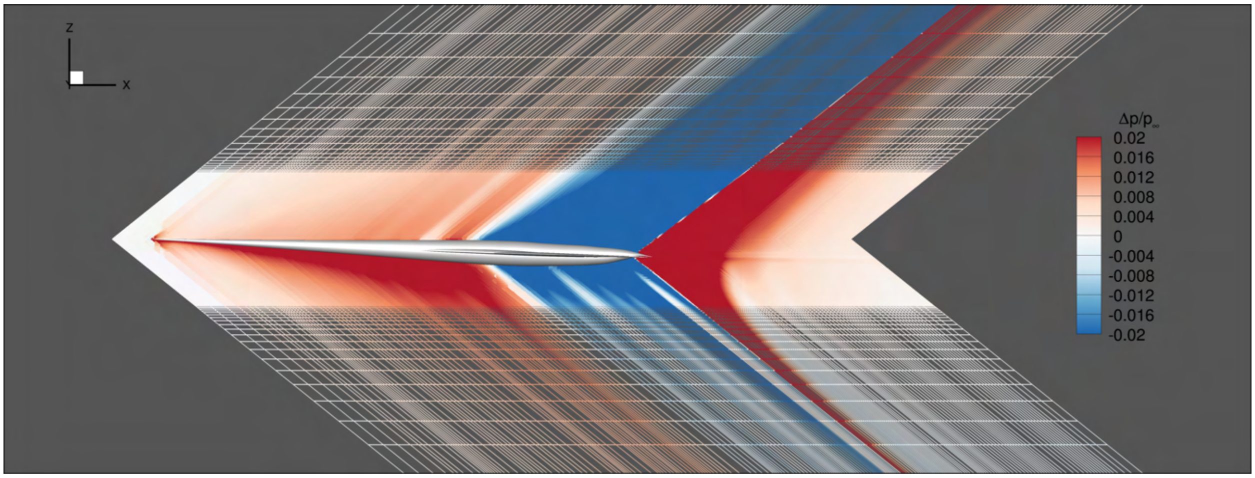

(a) Benchmark indicator adapted mesh.

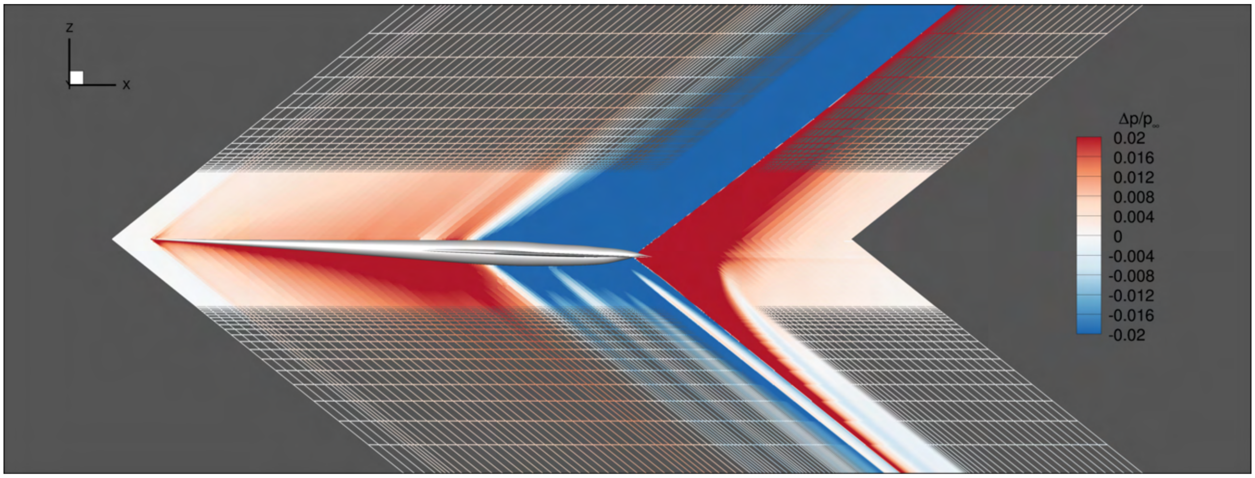

(b) Mach indicator adapted mesh.

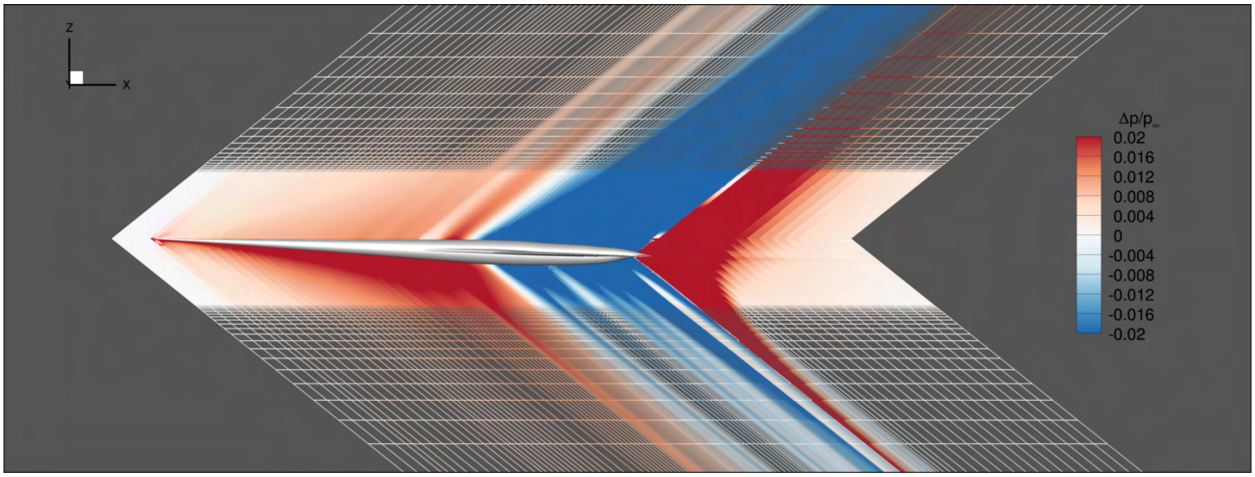

(c) Adjoint derived output-based indicator adapted mesh.

Fig. 9 Symmetry plane plot of the off-body adapted Mach cone aligned CFD meshes for the JAXA Wing Body colored by pressure disturbance.

propagated solutions are highlighted on $x = L_{\text{body}}$ slices of the space marching grid in Figure 10. The left side of the slice shows the difference between initial coarse and fine grid pressure signatures, with the right side comparing the benchmark adapted 10a, Mach adapted 10b, and output-based adapted 10c solution variance from the fine grid. Lines further from the body correspond to solution differences propagated from further upstream of the tail. Importantly, the magnitude of the difference of the output-based is significantly reduced compared to the coarse grid solution. The Mach adapted grid solution produces higher-magnitude differences in comparison to the adjoint adapted grid further upstream due to coarsening in the mid-section of the fuselage. Both benchmark and Mach adapted solutions produce differences of the same magnitude as the coarse grid solution, suggesting that over-refinement is occurring in regions not directly generating discretization errors. Higher overall improvement is obtained from the output-based adapted solution.

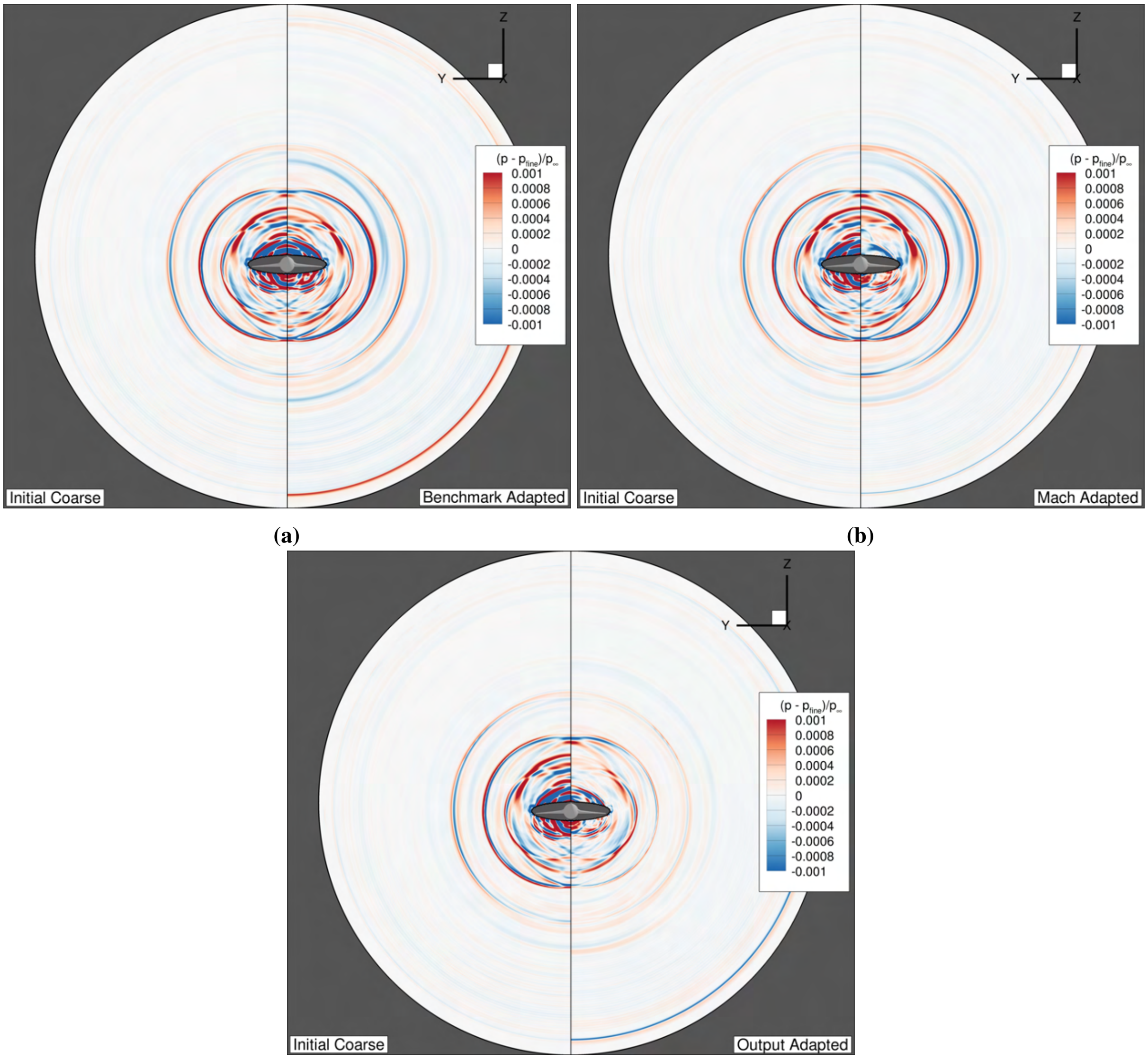

(a) **(b)**

(c)

Fig. 10 JAXA Wing-Body pressure differences between coarse and fine near-field space marching solutions at an x-slice location $x = L_{\text{body}}$. The left side of the slice shows the pointwise difference between the initial coarse grid and fine grid pressure compared to (a) benchmark adapted, (b) mach adapted, and (c) output-based adapted pressure differences on the right.

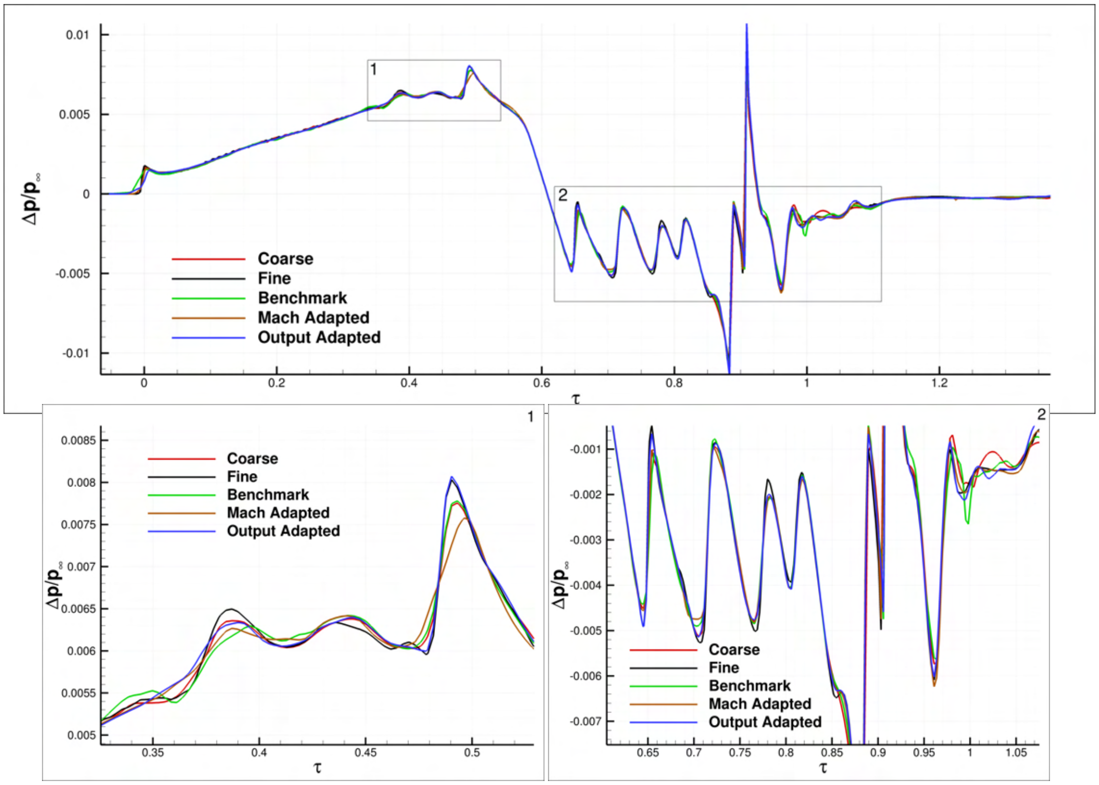

Fig. 11 JWB on-track pressure signature comparisons at $r/L_{\text{body}} = 1$.

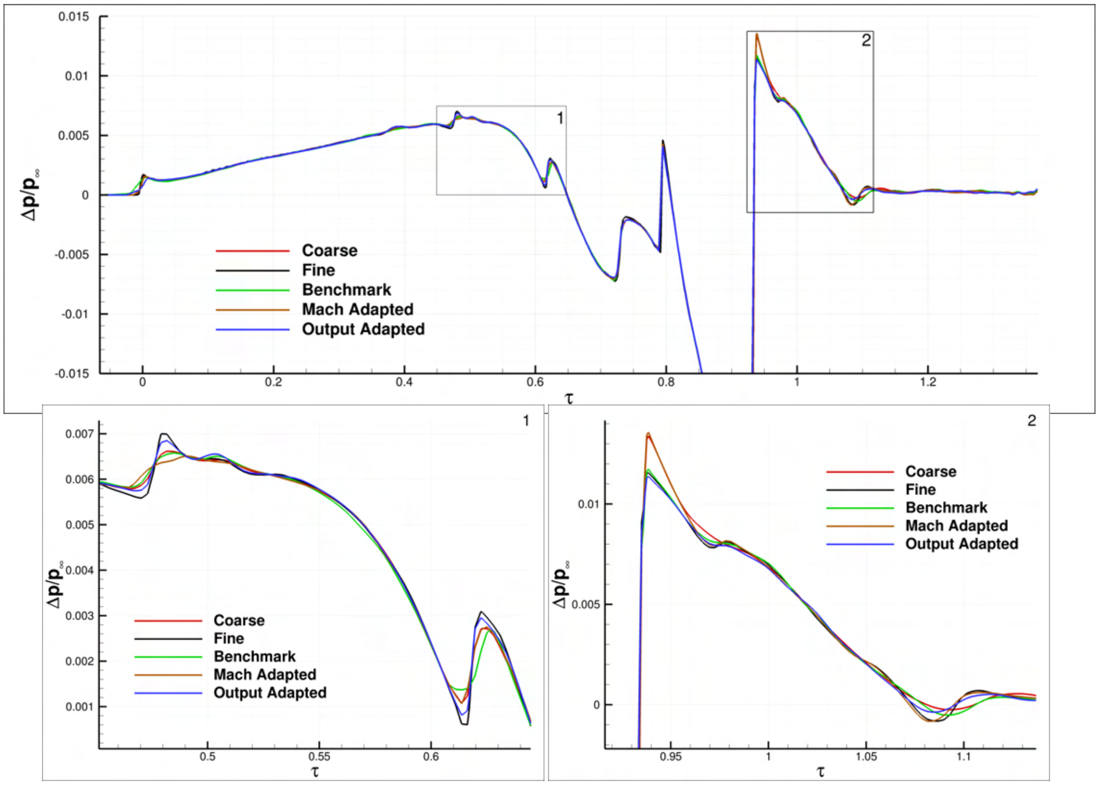

Fig. 12 JWB pressure signature comparisons at $r/L_{\text{body}} = 1$ and an off-track angle $\phi = 50°$.

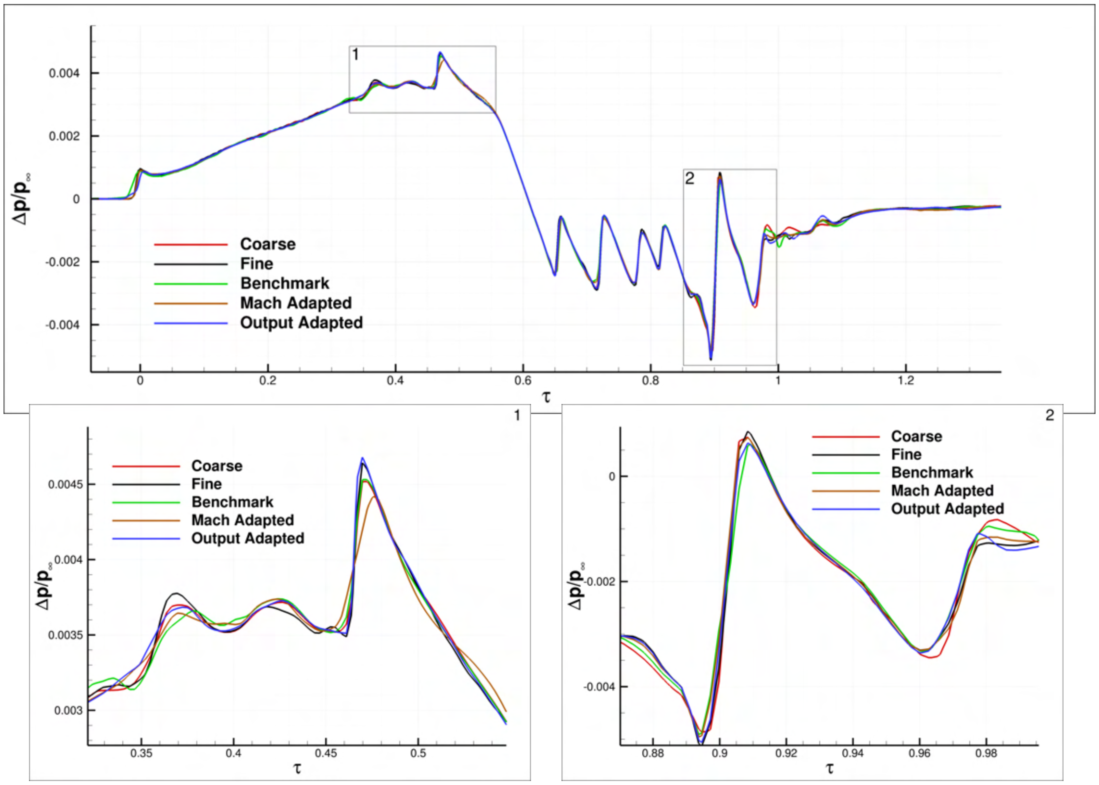

Fig. 13 JWB on-track pressure signature comparisons at $r/L_{\text{body}} = 3$.

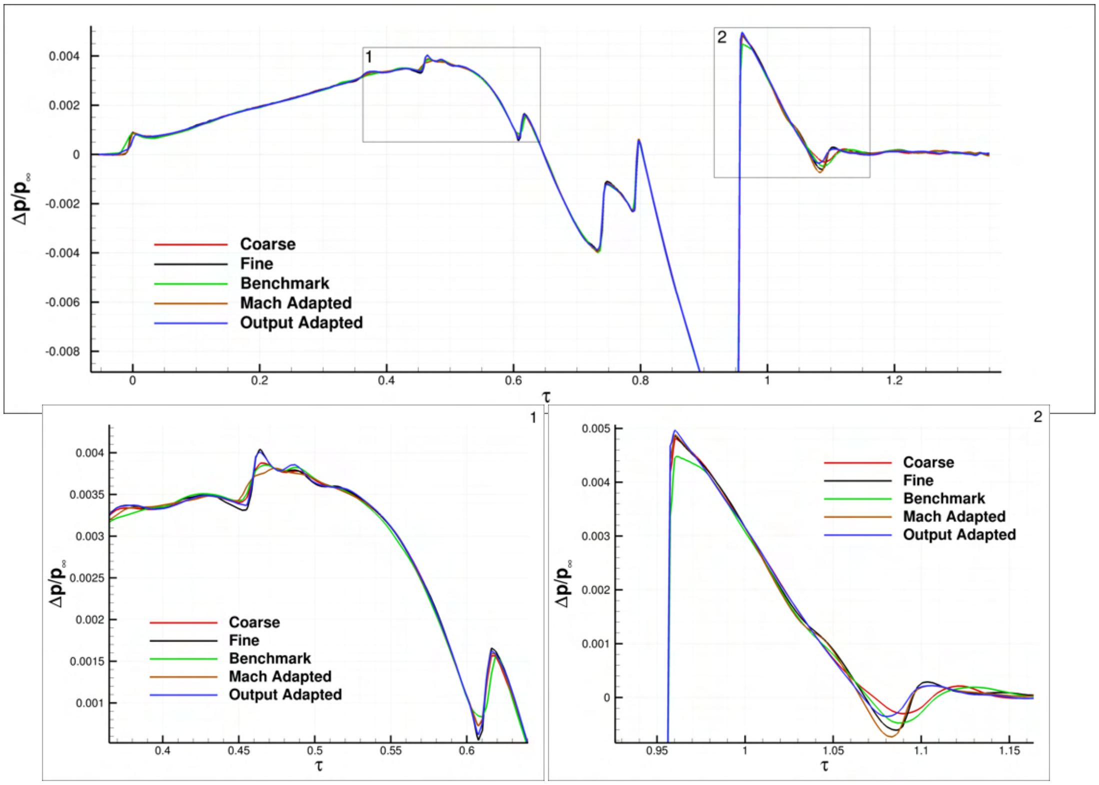

Fig. 14 JWB pressure signature comparisons at $r/L_{\text{body}} = 3$ and off-track angle $\phi = 50°$.

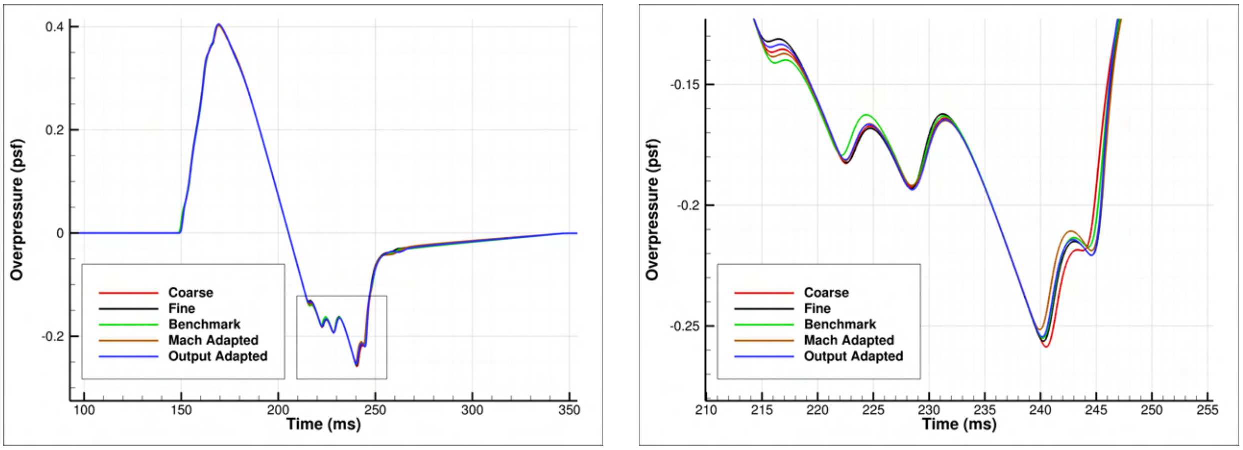

(a) Ground signature.

(b) Zoom-in of rectangular box.

Grid	ASEL [dB(A)]	BSEL [dB]	CSEL [dB(C)]	PL [dB]	ASEL Rel. Error	BSEL Rel. Error	CSEL Rel. Error	PL Rel. Error
Fine	62.15	75.96	90.78	75.98	-	-	-	-
Coarse	60.86	75.43	90.71	74.83	2.064%	0.692%	0.072%	1.514%
Benchmark	61.51	75.45	90.66	75.18	1.026%	0.673%	0.131%	1.045%
Mach Adapted	61.73	75.61	90.66	75.45	0.661%	0.457%	0.134%	0.699%
Output Adapted	62.37	75.86	90.74	76.10	**0.359%**	**0.132%**	**0.048%**	**0.161%**

Fig. 15 JWB overpressure ground signatures propagated from an on-track radial extraction location $r/L_{\mathbf{body}} = 3$ and their associated loudness metrics.

2. *Ground-level Signatures and Loudness Metrics*

Extracted pressure signatures from a radial distance $r/L_{\text{body}} = 3$ couple the space marching solution to the far-field propagation solver. Figure 15a shows the overpressure signature resulting from the propagated on-track waveform for each solution. The low-pressure and recovery portions of the N-wave show the largest variance between solutions, however, the output-based adapted and fine grid signatures are nearly identical as shown in Figure 15b. This results in the output-based adapted grid achieving the highest improvement in loudness metrics reported in Figure 15. Looking at the off-track signatures in Figure 16a, a similar story unfolds. Here, the recovery portion around 260 ms tends to have the highest variance, with the output-based adapted and fine grid signatures being the furthest apart. The high-pressure peak between 155-165 ms is again well-resolved, however, the low-pressure trough has notable variance, which is illustrated in Figure 16b. As with the on-track results, we see that the output-based adapted grid signature is closest to the fine grid signature. The benchmark and Mach signatures result in nearly identical loudness metrics, slightly improved over the output-based signature calculated BSEL. The output-based signature achieves higher accuracy ASEL and PL metric predictions than the other methodologies, while matching the accuracy of CSEL prediction obtained by the Mach adapted signature. Overall, the best improvement in coarse ground-level signatures and loudness metrics is achieved via output-based adaptation.

3. *Cost Analysis*

Computational cost for an adaptation cycle including the final flow restart has been presented in Table 1. Resource usage in CPU-hours for each JWB simulation performed on NASA's Electra supercomputer using five Skylake nodes, each containing two 20-core Xeon Gold 6148 sockets (2.4 GHz). Reported connectivity time is the total time of two connectivity runs, initial and post-adaptation. The restarted flow solve is a warm-restart using the solution from the primal solve interpolated onto the adapted grid. The cost of adapting the off-body grid using an output-based indicator only accounted for less than 3.4% of the total cost of an adaptation cycle, which was dominated by the initial primal solve and final restart. This demonstrates the choice of the first-order adjoint solver that was described in Section IV.A. The average adaptation time across the various indicators accounts for only 1% of the total average combined cost of initial primal flow solves and final restarts. This results in an average cost increase of 21.7% over the initial coarse grid primal solve and a 43.5% reduction in cost compared to solving on the automatically generated fine mesh.

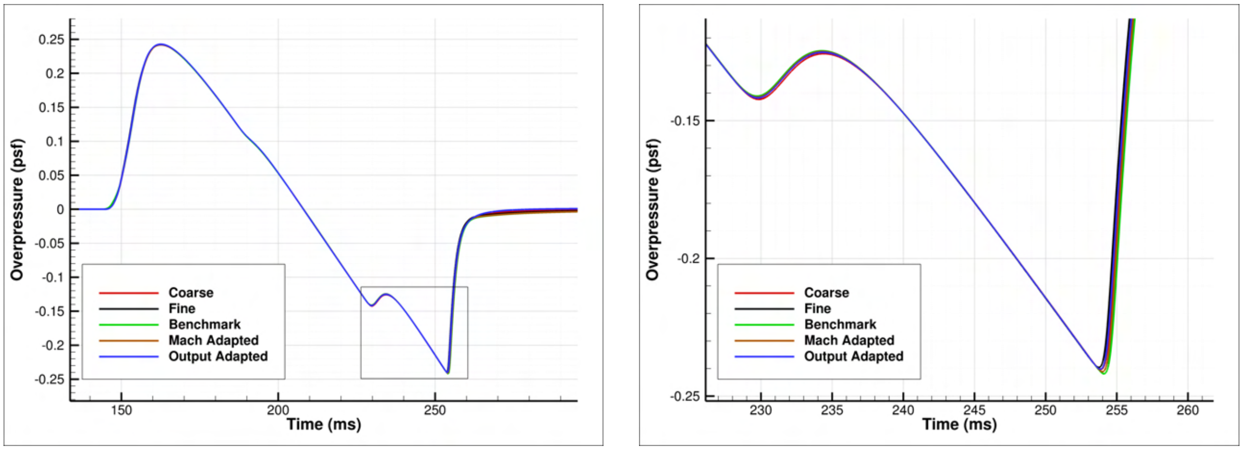

(a) Ground signature. **(b) Zoom-in of rectangular box.**

Grid	ASEL [dB(A)]	BSEL [dB]	CSEL [dB(C)]	PL [dB]	ASEL Rel. Error	BSEL Rel. Error	CSEL Rel. Error	PL Rel. Error
Fine	62.32	76.75	89.07	77.34	-	-	-	-
Coarse	62.18	76.66	89.05	77.22	0.230%	0.120%	0.022%	0.173%
Benchmark	62.40	76.77	89.07	77.42	0.134%	**0.027%**	**0.004%**	0.102%
Mach Adapted	62.39	76.79	89.08	77.42	0.108%	0.050%	0.016%	0.099%
Output Adapted	62.27	76.69	89.08	77.27	**0.080%**	0.077%	/0.011%	**0.088%**

Fig. 16 JWB overpressure ground signatures propagated from a radial extraction location $r/L_{\text{body}} = 3$ at an off-track angle $\phi = 50°$ and their associated loudness metrics, with the minimum relative difference in bold.

Table 1 Resource usage in CPU-hours for each JWB simulation performed on NASA's Electra supercomputer using five Skylake nodes, each containing two 20-core Xeon Gold 6148 sockets (2.4 GHz).

Grid	Connectivity	Primal Solve	Adjoint Solve	Embedding	Adaptation	Restart	**Total**
Coarse	0.14	25.46	-	-	-	-	**25.60**
Benchmark Adapted	0.28	25.46	-	-	0.02	4.70	**30.46**
Mach Adapted	0.29	25.46	-	-	0.01	5.66	**31.42**
Output Adapted	0.28	25.46	0.87	0.17	0.03	5.03	**31.56**
Fine	0.13	55.99	-	-	-	-	**56.12**

C. X-59 C608 Demonstrator Model

The X-59 C608 demonstrator model was a part of the Third AIAA SBPW. Various perspectives of its geometry are shown in Figure 8. This 27.432 meter long aircraft is designed for flight at Mach 1.4 at an angle of attack 2.15° with a cruise altitude of 16.22km. Standard atmospheric conditions are assumed, with a freestream temperature of $389.9°R$. These high-altitude cruise flight conditions result in a flight Reynolds number of 109,776 per inch.

Unlike the JWB case, intakes and exhaust ducts are modeled on this aircraft, all of which are treated as inflow and outflow boundary conditions to the CFD domain. Air intakes are prescribed subsonic inflow and outflow boundary conditions that specify static pressure and extrapolate all other states. Engine exhaust boundary conditions are determined by setting stagnation pressure and temperature that prescribe all states using isentropic flow equations. These boundary conditions include the engine fan face where $p_{\text{static}}/p_{\text{static,fs}} = 2.6$, the environmental control system (ECS) inlet face with $p_{\text{static}}/p_{\text{static,fs}} = 1.4$, the engine exhaust plenum chamber where $p_{\text{total}}/p_{\text{static,fs}} = 10.0$ and $T_{\text{total}}/T_{\text{static,fs}} = 7.0$, and the engine bypass exhaust with $p_{\text{total}}/p_{\text{static,fs}} = 2.4$ and $T_{\text{total}}/T_{\text{static,fs}} = 2.0$ [16].

A CFD mesh refinement study was performed during the workshop, and the coarse grid system, which was deemed sufficient based on that study, is used for all reported results [16]. The automatically generated off-body grid has a streamwise domain length of $1.82\,L_{\text{body}}$ and circumferential extent of 180° discretized with uniform spacing into $N_s = 257$ streamwise and $N_\theta = 181$ circumferential points, respectively. Finally, a stretching ratio of $SR = 1.2$ and maximum aspect ratio of $AR_{\max} = 20$ are applied in the radial direction, with a domain extent $r_{\max} = 0.53\,L_{\text{body}}$

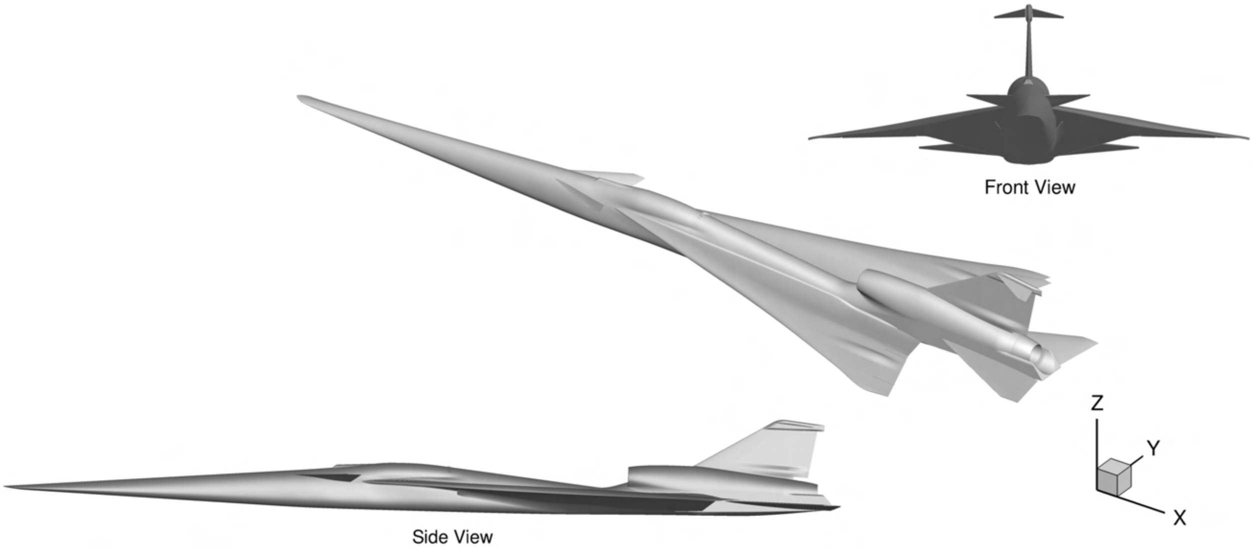

Fig. 17 X-59 C608 geometry from the Third AIAA Sonic Boom Prediction Workshop.

discretized into $N_r = 51$ points. The coarse grid has $29M$ total nodes, of which 2,154,688 nodes comprise the off-body grid. The fine grid is constructed by uniformly refining the off-body grid in the streamwise and circumferential directions with refinement factor $r_f = 2$, resulting in 8,569,152 nodes.

Adaptation is performed on the coarse mesh using a mach number feature-based, output-based, and benchmark adaptation indicators. All adaptation parameters are automatically set according to our determined best practices to $\beta = \tanh^{-1}(0.8)/4\,\bar{g}$ and $A = 10$. Only one adaptation cycle has been performed for each indicator, since it was found that multiple adaptation cycles do not result in additional improvements over a single cycle. The RANS equations are solved using a third-order upwind flux with a Koren limiter and SA-RC-QCR2000 turbulence model. The final adapted coarse grids are shown in Figure 9 colored by pressure disturbance $\Delta p/p_\infty$.

The adapted CFD grid solutions are space marched from the near-field to the mid-field using LAVA's high-fidelity space marching solver. We apply the best practices established from the JWB geometry by Housman et al. [17]. The space marching grid domain extends 5 body lengths and is discretized into 36,145,338 nodes. The three-dimensional Euler equations are discretized using a fourth-order Hybrid Weighted Compact Nonlinear scheme with fifth-order WENO interpolation in the non-space marching direction and second-order backward differentiation is used in the space marching direction. The two-dimensional nonlinear system is solved at each space marching station using an alternating line Jacobi relaxation. Line probes are extracted from the converged space marching solution at radial distances $r/L_{\text{body}} = 3$.

1. Near-field Signature Results

The extracted near-field signatures for on-track and off-track angles are shown in Figures 20 and 21. For both angles, the largest waveform improvements occur for $0.4 \leq \tau \leq 0.6$ and in the plume region, $\tau > 1$. The waveform sensitivities for $0.4 \leq \tau \leq 0.6$ are likely caused by the ECS inlets. Similar to the JWB case, we see that the benchmark adapted serves as a conservative lower bound on the performance of the adaptation procedure. This demonstrates the ability of feature-based and output-based adaptation indicators to target sources of discretization error. For this more complex geometry, the adjoint sensitivity in the nose and tail shock regions are of comparable magnitude, unlike the results shown for the JWB case. Instead of degrading the accuracy of the nose shock waveform, output based adaptation improves the accuracy of the nose shock to a level nearly identical to the one resulting from feature-based adaptation. Qualitatively, we do not see large differences in the signatures. However, from the zoom boxes of Figure 20, it is apparent that the adapted grids are achieving accuracy levels closer to that of the fine grid. From the mathematical derivation in Section IV.A, we do not expect the output-based adaptation to exceed the accuracy threshold of the fine grid.

The examination of only two pressure traces is insufficient to draw conclusions on the improvement of the space marched solutions. Figure 19 shows pressure differences between coarse and fine near-field space marching solutions at a streamwise location $x = L_{\text{body}}$. The left side of each slice shows the pointwise difference between the initial coarse

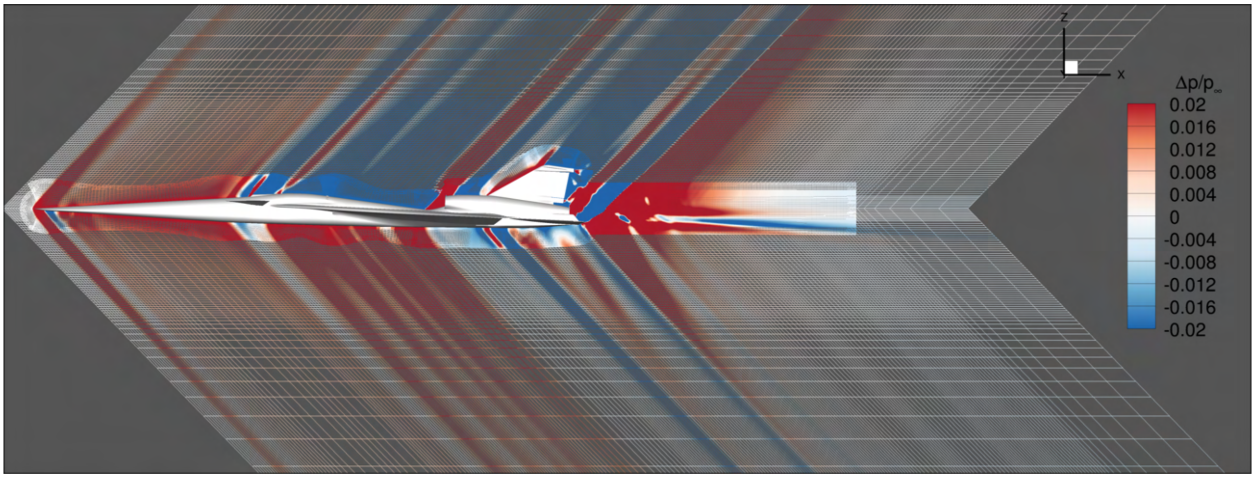

(a) Benchmark indicator adapted mesh.

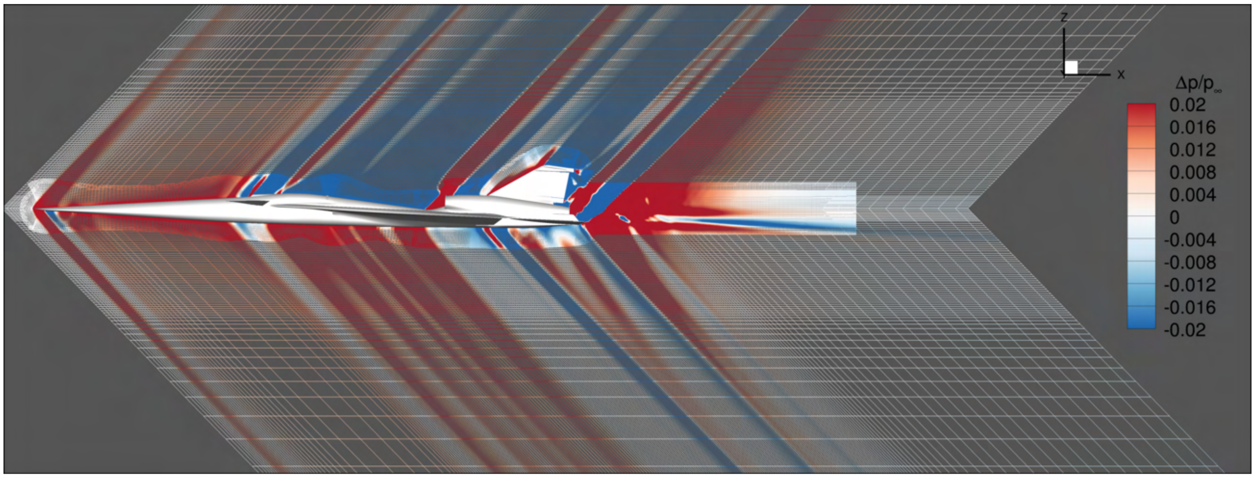

(b) Mach indicator adapted mesh.

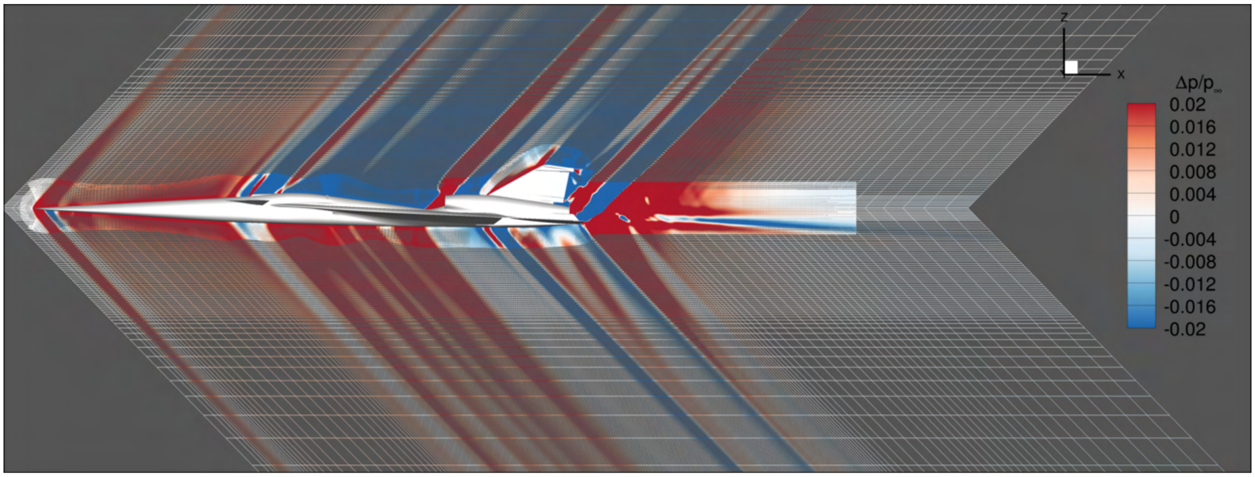

(c) Adjoint derived output-based indicator adapted mesh.

Fig. 18 Symmetry plane plot of the off-body adapted Mach cone aligned CFD meshes for the X-59 C608 geometry, colored by pressure disturbance.

grid and fine grid pressure compared to benchmark 19a, mach 19b, and output 19c adapted pressure differences on the right. We see significant reduction of the magnitude of all off-track errors. As seen in the pressure traces, the benchmark indicator yields the lowest improvement in accuracy.

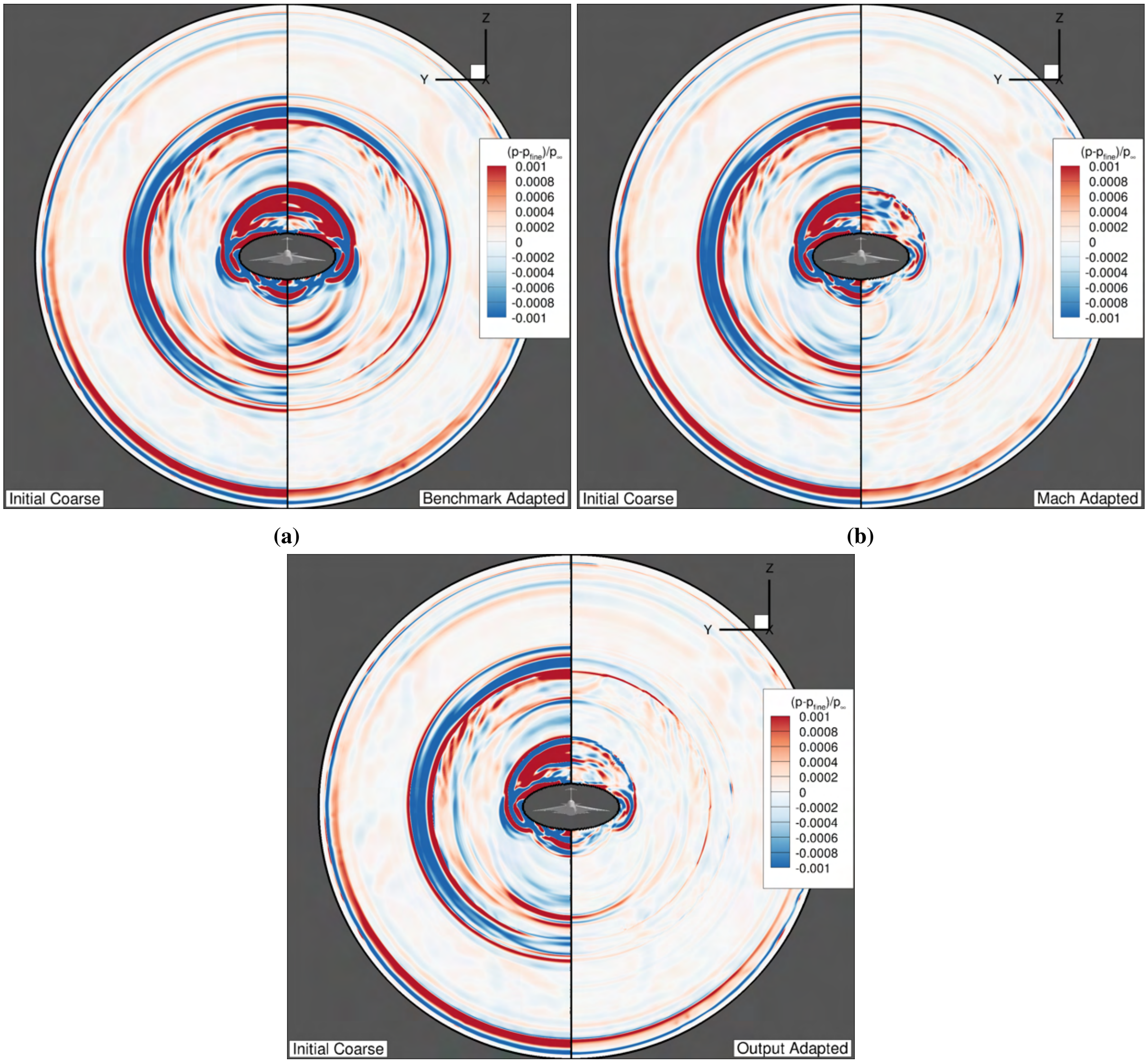

(a)

(b)

(c)

Fig. 19 C608 pressure differences between coarse and fine near-field space marching solutions at an x-slice location $x = L_{\text{body}}$. The left side of the slice shows the pointwise difference between the initial coarse grid and fine grid pressure compared to (a) benchmark adapted, (b) mach adapted, and (c) output-based adapted pressure differences on the right.

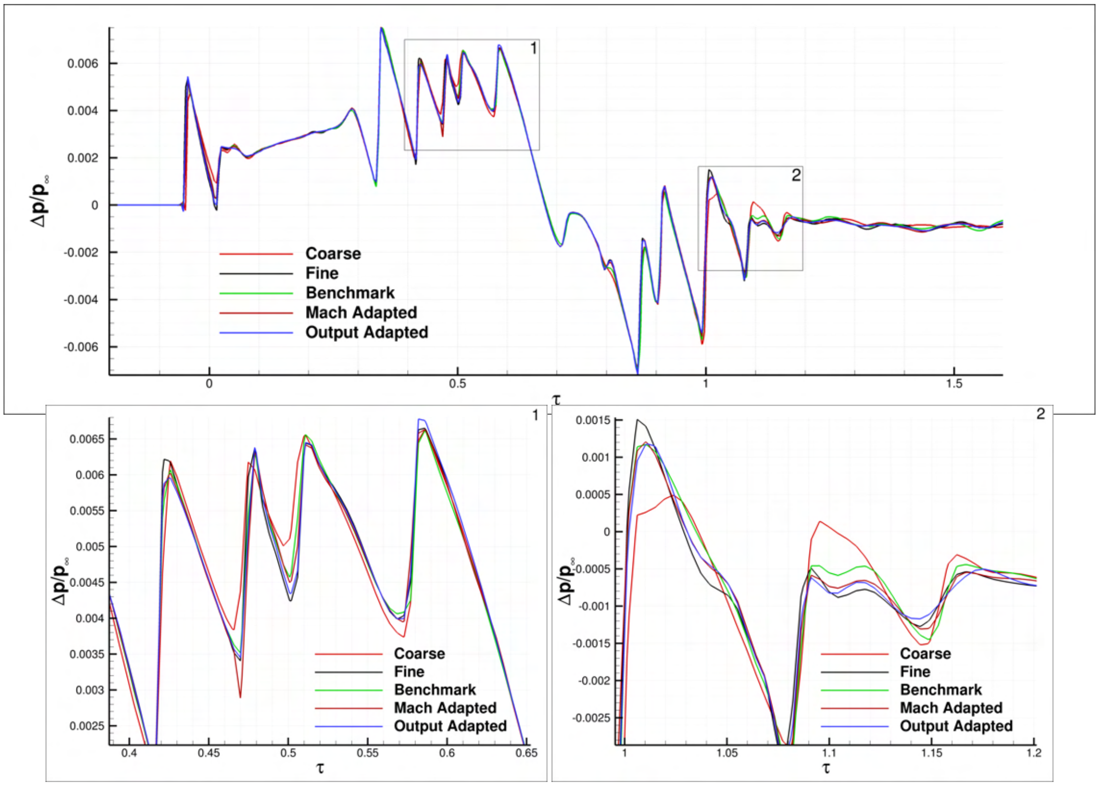

Fig. 20 C608 on-track pressure signature comparisons at $r/L_{\mathrm{body}} = 3$.

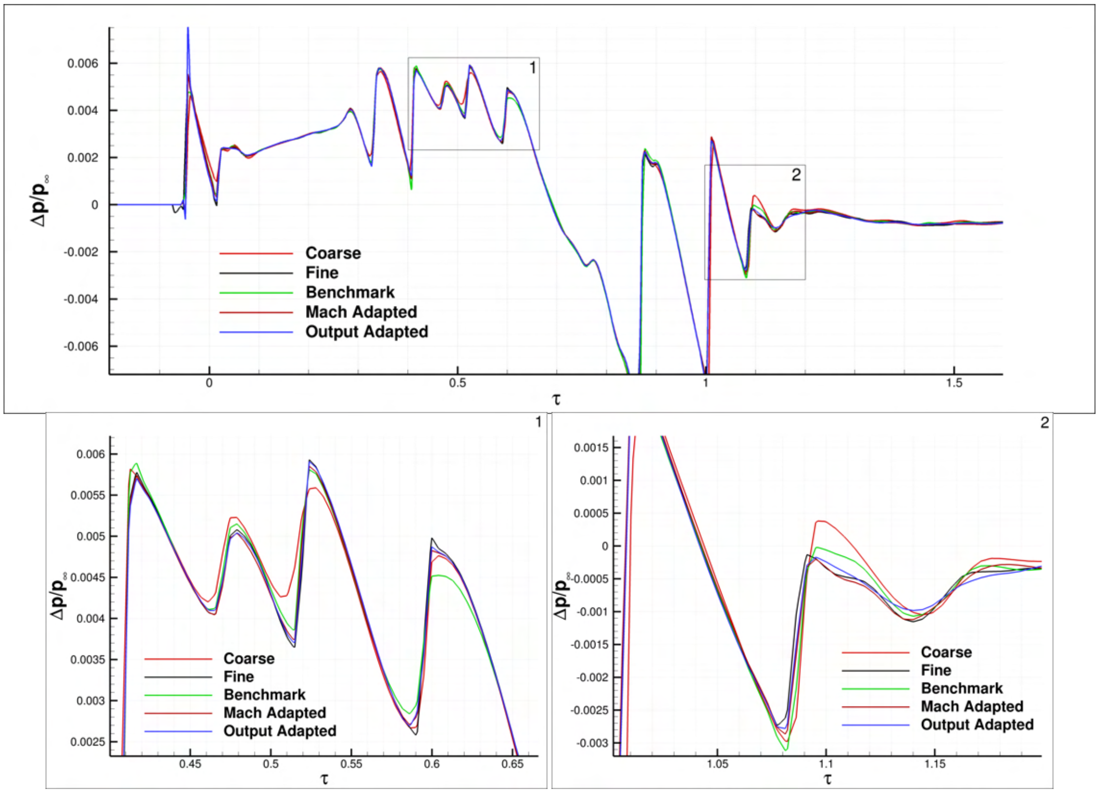

Fig. 21 C608 pressure signature comparisons at $r/L_{\mathrm{body}} = 3$ and an off-track angle of $\phi = 30°$.

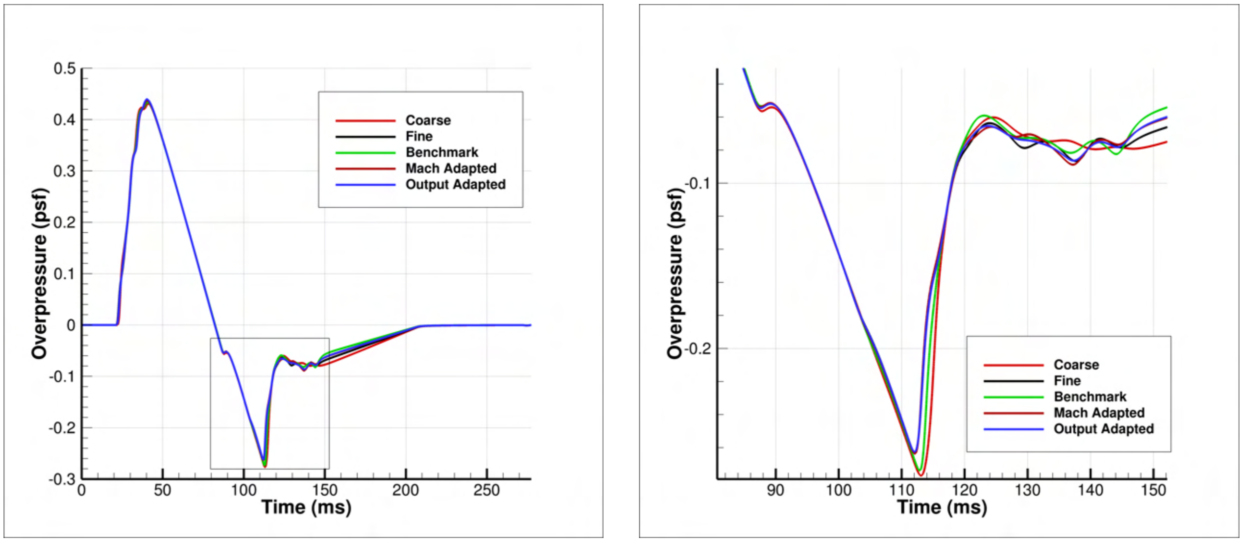

(a) Ground signature. **(b) Zoom-in of rectangular box.**

Grid	ASEL [dB(A)]	BSEL [dB]	CSEL [dB(C)]	PL [dB]	ASEL Rel. Error	BSEL Rel. Error	CSEL Rel. Error	PL Rel. Error
Fine	62.21	76.49	91.27	76.53				
Coarse	63.40	77.78	91.72	77.80	1.917%	1.692%	0.497%	1.660%
Benchmark	62.80	77.22	91.53	77.41	0.946%	0.952%	0.285%	1.149%
Mach Adapted	62.63	76.73	91.29	76.94	0.664%	0.312%	**0.025%**	0.544%
Output Adapted	62.11	76.53	91.30	76.45	**0.160%**	**0.056%**	0.032%	**0.103%**

Fig. 22 C608 overpressure ground signatures propagated from an on-track radial extraction location $r/L_{\text{body}} = 3$ and their associated loudness metrics.

2. *Ground-level Signatures and Loudness Metrics*

The extracted pressure cylinder at $r/L_{\text{body}} = 3$ couple the space marching solution to the far-field propagation solver. Figures 22 and 23 show ground-level overpressure signatures and loudness metrics corresponding to the propagated near-field waveforms shown in Figures 20 and 21, respectively. Ground-level signature accuracy improvements are evident in the low-pressure and recovery portions between 110 – 150 ms. The output and mach adapted overpressure signatures are indistinguishable, while the benchmark adaptation provides little benefit over the coarse grid.

To understand the impact of the increased accuracy present in the N-wave owing to the adaptation algorithm, we rely on the loudness metrics. Tables 22 and 23 contain the loudness metrics and their relative difference from the fine grid predictions. At the on-track angle, adapted grid metrics are reduced to less than 0.4% relative error. Of these errors, ASEL, BSEL, and PL are minimized by output adaptation to an error of less than 0.2%. However, the CSEL coarse grid error is minimized by solution based adaptation to 0.025%. For the off-track angle, $\phi = 30°$, output based adaptation minimizes all the relative metric errors. The greatest reductions are in ASEL and PL, resulting in relative errors of 0.973% and 0.783%, respectively.

3. *Cost Analysis*

For complex geometries, often a number of large near-body grids are required and may account for the majority of the degrees of freedom in the grid system. In fact, the C608 off-body grid only accounts for 23.59% of fine grid system. Therefore, the computational resource savings of using an adapted off-body grid are minimal compared to a fine uniform off-body grid. The primary advantage of this methodology is robustness to flight plan changes. As the flow field changes in the off-body region, the mesh adaptation is able to ensure accurate capturing of major flow features. Evidence of this was presented in Figure 18.

To analyze the cost of the coarse grid adaptation, we compare our results to those generated by a structured curvilinear overset mesh established as the LAVA best practice grid during the Third AIAA SBPW. The off-body grid was manually generated with user-specified local refinement regions. Reported results and a more detailed description were published

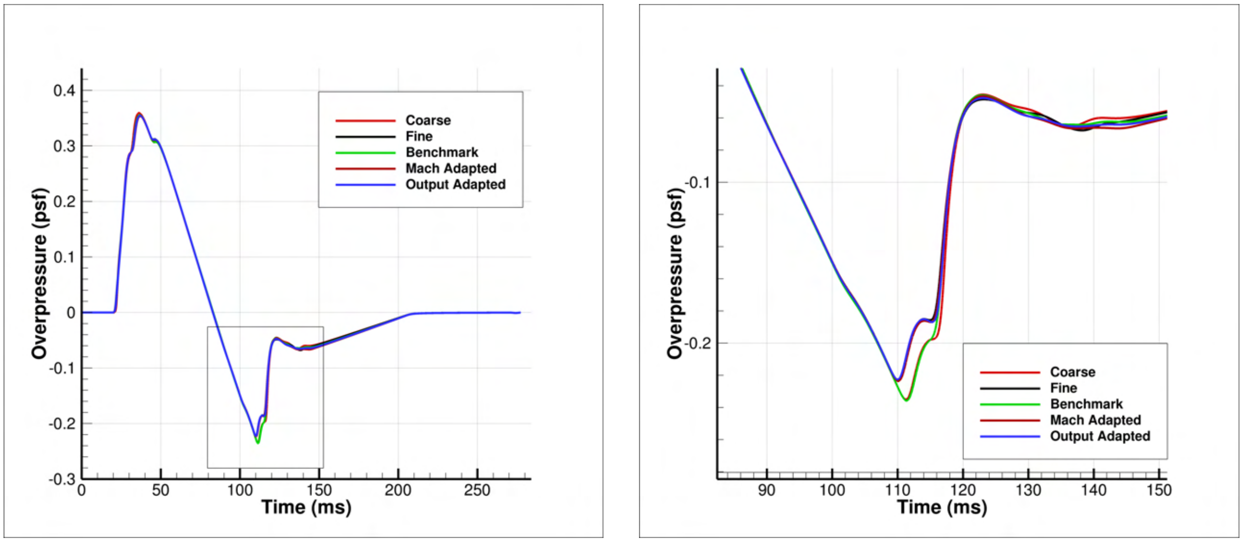

(a) Ground signature **(b) Zoom-in of rectangular box**

Grid	ASEL [dB(A)]	BSEL [dB]	CSEL [dB(C)]	PL [dB]	ASEL Rel. Error	BSEL Rel. Error	CSEL Rel. Error	PL Rel. Error
Fine	60.14	75.51	89.90	74.51				
Coarse	61.80	76.34	90.29	76.24	2.753%	1.098%	0.432%	2.321%
Benchmark	60.91	76.18	90.22	75.58	1.287%	0.887%	0.363%	1.446%
Mach Adapted	60.85	75.90	89.99	75.25	1.179%	0.510%	0.103%	0.994%
Output Adapted	60.73	75.77	89.95	75.09	**0.973%**	**0.342%**	**0.057%**	**0.783%**

Fig. 23 C608 overpressure ground signatures propagated from an off-track angle of $\phi = 30°$ and radial extraction location $r/L_{\text{body}} = 3$ and their associated loudness metrics. The relative difference from the fine grid metrics is computed for each methodology, with the minimum difference in bold.

by Duensing et al. [16]. For comparisons of wall time, each case has comparable nodes per core ratios. A breakdown of the load balancing for each case is presented in Table 2.

First, we establish the accuracy relative to the reference grid. Loudness metric comparisons are made in Tables 4 and 5 with relative errors computed with respect to the reference grid. The minimal relative error between coarse grids is bold for each loudness metric. Analysis shows favorable comparisons between coarse adapted and reference grid metrics. On-track BSEL, CSEL, and PL metrics are minimized by the mach adapted grid. We see for BSEL and PL that feature-based adaptation performs better than the fine grid, reaching error levels of 0.002% and 0.174%, respectively. Furthermore, output-based adaptation minimizes the ASEL error to 0.855%, which is lower than that of the fine grid. The reported ASEL, BSEL, and PL metrics at $\phi = 30°$ are minimized by the output-adapted grid. We see that the coarse adapted grids are able to produce higher accuracy BSEL and CSEL predictions than the fine grid, reaching error levels of less than 0.18%.

The reference grid CFD simulation was performed using 400 cores and took 1.4 hours of wall-time, incurring a cost of 18.3 standard billing units (SBUs). The coarse grid solution used only 80 cores and cost 4.6 SBUs compared to the 6.7 SBUs for the fine grid solution. Output-based adaptation cycle costs an additional 0.3 SBUs over the initial coarse grid and other adaptation methodologies, since we require an adjoint linear solve to form our error indicator in (25). Notably, the cost of restarts remains fixed. We contribute this to the similarities between the adapted grids themselves and the accuracy of the interpolations post-adaptation to generate a valid restart file. In summary, adaptation results in error levels below 2.8% while providing a greater than a 3.73× reduction in cost.

Table 2 Load balancing for C608

Grid	Total Nodes*	Degrees of Freedom*	Nodes per Core
Reference	161.990	127.379	318,448
Fine	36.329	23.613	295,166
Coarse	29.754	20.874	260,925

*In millions.

Table 3 Resource usage in wall-time and standard billing units (SBU) for each C608 simulation.

Grid	Connectivity	Primal Solve	Adjoint Solve	Embedding	Adaptation	Restart	**Total**	SBU
Reference	-	1.4	-	-	-	-	1.4	**18.3**
Coarse	0.02	1.59	-	-	-	-	1.77	**4.6**
Fine	0.02	2.60	-	-	-	-	2.62	**6.7**
Benchmark Adapted	0.04	1.59	-	-	-	0.14	1.77	**4.6**
Mach Adapted	0.04	1.59	-	-	-	0.14	1.77	**4.6**
Output Adapted	0.04	1.59	0.10	0.01	0.01	0.14	1.89	**4.9**

Table 4 On-track C608 loudness metrics compared to reference grid.

Grid	ASEL [dB(A)]	BSEL [dB]	CSEL [dB(C)]	PL [dB]	ΔASEL	ΔBSEL	ΔCSEL	ΔPL
Reference	61.59	76.73	91.20	76.81	-	-	-	-
Fine	62.21	76.49	91.27	76.53	1.017%	0.309%	0.076%	0.368%
Coarse	63.40	77.78	91.72	77.80	2.953%	1.378%	0.574%	1.286%
Benchmark	62.80	77.22	91.53	77.41	1.972%	0.640%	0.361%	0.777%
Mach Adapted	62.63	76.73	91.29	76.94	1.687%	**0.002%**	**0.101%**	**0.174%**
Output Adapted	62.11	76.53	91.30	76.45	**0.855%**	0.254%	0.108%	0.470%

Table 5 Off-track C608 loudness metrics compared to reference grid.

Grid	ASEL [dB(A)]	BSEL [dB]	CSEL [dB(C)]	PL [dB]	ΔASEL	ΔBSEL	ΔCSEL	ΔPL
Reference	59.09	75.64	89.98	74.42	-	-	-	-
Fine	60.14	75.51	89.90	74.51	1.782%	0.186%	0.086%	0.122%
Coarse	61.80	76.34	90.29	76.24	4.584%	0.928%	0.346%	2.447%
Benchmark	60.91	76.18	90.22	75.58	3.092%	0.718%	0.277%	1.570%
Mach Adapted	60.85	75.90	89.99	75.25	2.982%	0.341%	**0.017%**	1.117%
Output Adapted	60.73	75.77	89.95	75.09	**2.772%**	**0.173%**	0.029%	**0.906%**

VI. Conclusion

An automatic Mach cone aligned off-body grid generation algorithm for structured curvilinear overset grid systems was presented. The ability for this automated algorithm to increase the accuracy for a user-specified number of nodes in the off-body domain was shown for the JWB geometry and X-59 C608 demonstrator model. Comparisons were made between a feature-based, output-based, and a conservative benchmark indicator. Combined with its associated error metric for an output quantity of interest, output-based indicators may be a favorable choice over the feature-based. However, both adaptation indicators were demonstrated to provide fine grid level accuracy at a fixed coarse grid cost. The automation of the algorithm allows for capturing of important physical features, allowing this approach to be robust to flight plan changes. Future work is underway to provide mesh redistribution to the near-body overset grids, introducing further automation and CFD discretization error minimization.

Acknowledgments

This work was partially supported by NASA's Aeronautics Research Mission Directorate (ARMD) Commercial Supersonic Technologies (CST) and Transformational Tools and Technologies (TTT) projects. The authors would like to express their gratitude to Brandon Lowe for his invaluable contributions in the development of the LAVA adjoint solver. We would also like to acknowledge the exceptional efforts of the LAVA team, particularly Scott Neuhoff, James Jensen, James Koch, and Emre Sozer. Special thanks are due to Marian Nemec from NASA Ames Research Center for his expert technical guidance and insightful discussions. We are also grateful to Gaetan Kenway for his diligent supervision of the code development. Moreover, the authors would like to extend a special acknowledgement to Cetin Kiris, whose exceptional leadership and technical guidance were crucial in shaping the LAVA team and the trajectory of this project. Results in this article are from the doctoral dissertation of the first author to be submitted in partial fulfillment of the requirements for a PhD in mathematics at the University of Kentucky. We would like to thank Peter Hislop from the University of Kentucky and Christoph Brehm from the University of Maryland for their academic advisory roles. Computer time has been provided by NASA's Advanced Supercomputing (NAS) facility at NASA Ames Research Center.

References

[1] Alauzet, F., and Loseille, A., "High Order Sonic Boom Modeling by Adaptive Methods," *Journal of Computational Physics*, Vol. 229, 2010, pp. 561–593. https://doi.org/10.1016/j.jcp.2009.09.020.

[2] Wintzer, M., Nemec, M., and Aftosmis, M., *Adjoint-Based Adaptive Mesh Refinement for Sonic Boom Prediction*, 2012.

[3] Nemec, M., and Aftosmis, M., "Toward Automatic Verification of Goal-Oriented Flow Simulations," 2014.

[4] Rallabhandi, S. K., and Park, M. A., *Adjoint-Based Mesh Adaptation for the Sonic Boom Signature Loudness*, 2017. https://doi.org/10.2514/6.2017-3049, URL https://arc.aiaa.org/doi/abs/10.2514/6.2017-3049.

[5] Anderson, G. R., Aftosmis, M. J., and Nemec, M., "Cart3D Simulations for the Second AIAA Sonic Boom Prediction Workshop," *Journal of Aircraft*, Vol. 56, No. 3, 2019, pp. 896–911.

[6] Nemec, M., Aftosmis, M., Rallabhandi, S., and Rodriguez, D., "Goal-Oriented Discretization Error Control in Coupled Nearfield-Farfield Low-Boom Simulations," 2022. https://doi.org/10.2514/6.2022-4085.

[7] Fidkowski, K. J., and Darmofal, D. L., "Review of Output-Based Error Estimation and Mesh Adaptation in Computational Fluid Dynamics," *AIAA Journal*, Vol. 49, No. 4, 2011, pp. 673–694. https://doi.org/10.2514/1.J050073, URL https://doi.org/10.2514/1.J050073.

[8] Alauzet, F., and Loseille, A., "A decade of progress on anisotropic mesh adaptation for computational fluid dynamics," *Computer-Aided Design*, Vol. 72, 2016, pp. 13–39. https://doi.org/https://doi.org/10.1016/j.cad.2015.09.005, URL https://www.sciencedirect.com/science/article/pii/S0010448515001517, 23rd International Meshing Roundtable Special Issue: Advances in Mesh Generation.

[9] Vanharen, J., Loseille, A., Alauzet, F., and Park, M. A., *Nearfield Anisotropic Mesh Adaptivity for the Third AIAA Sonic Boom Workshop*, 2022. https://doi.org/10.2514/6.2021-0347, URL https://arc.aiaa.org/doi/abs/10.2514/6.2021-0347.

[10] Park, M. A., Loseille, A., Krakos, J. A., and Michal, T. R., *Comparing Anisotropic Output-Based Grid Adaptation Methods by Decomposition
*, 2015. https://doi.org/10.2514/6.2015-2292, URL https://arc.aiaa.org/doi/abs/10.2514/6.2015-2292.

[11] Park, M. A., Barral, N., Ibanez, D., Kamenetskiy, D. S., Krakos, J. A., Michal, T. R., and Loseille, A., *Unstructured Grid Adaptation and Solver Technology for Turbulent Flows*, 2018. https://doi.org/10.2514/6.2018-1103, URL https://arc.aiaa.org/doi/abs/10.2514/6.2018-1103.

[12] Galbraith, M. C., Caplan, P. C., Carson, H. A., Park, M. A., Balan, A., Anderson, W. K., Michal, T., Krakos, J. A., Kamenetskiy, D. S., Loseille, A., Alauzet, F., Frazza, L., and Barral, N., "Verification of Unstructured Grid Adaptation Components," *AIAA Journal*, Vol. 58, No. 9, 2020, pp. 3947–3962. https://doi.org/10.2514/1.J058783, URL https://doi.org/10.2514/1.J058783.

[13] Rangarajan, A. M., May, G., and Dolejsi, V., *Adjoint-based anisotropic mesh adaptation for Discontinuous Galerkin Methods Using a Continuous Mesh Model*, 2017. https://doi.org/10.2514/6.2017-3100, URL https://arc.aiaa.org/doi/abs/10.2514/6.2017-3100.

[14] Meredith, K., Dahlin, J., Graham, D., Malone, M., Haering, E., Page, J., and Plotkin, K., *Computational Fluid Dynamics Comparison and Flight Test Measurement of F-5E Off-Body Pressures*, 2005. https://doi.org/10.2514/6.2005-6, URL https://arc.aiaa.org/doi/abs/10.2514/6.2005-6.

[15] Housman, J. A., Sozer, E., and Kiris, C. C., *LAVA Simulations for the First AIAA Sonic Boom Prediction Workshop*, 2008. https://doi.org/10.2514/6.2014-2008, URL https://arc.aiaa.org/doi/abs/10.2514/6.2014-2008.

[16] Duensing, J. C., Jensen, J. C., Housman, J. A., Piotrowski, M. G., Kenway, G. K., Maldonado, D., Sozer, E., and Kiris, C. C., *Structured Overset and Unstructured Grid Simulations for the Third AIAA Sonic Boom Prediction Workshop*, 2021. https://doi.org/10.2514/6.2021-0471, URL https://arc.aiaa.org/doi/abs/10.2514/6.2021-0471.

[17] Housman, J., Kenway, G., Jensen, J., and Kiris, C., "Efficient Near-Field to Mid-Field Sonic Boom Propagation Using a High-Order Space Marching Method," 2019. https://doi.org/10.2514/6.2019-3487.

[18] Kiris, C. C., Housman, J. A., Barad, M. F., Brehm, C., Sozer, E., and Moini-Yekta, S., "Computational framework for Launch, Ascent, and Vehicle Aerodynamics (LAVA)," *Aerospace Science and Technology*, Vol. 55, 2016, pp. 189–219. https://doi.org/https://doi.org/10.1016/j.ast.2016.05.008, URL https://www.sciencedirect.com/science/article/pii/S127096381630178X.

[19] Housman, J., Kenway, G., Jensen, J., and Kiris, C., "Algorithmic Improvements to a High-Order Space Marching Method for Sonic Boom Propagation," ICCFD, 2022.

[20] Rallabhandi, S. K., "Advanced Sonic Boom Prediction Using the Augmented Burgers Equation," *Journal of Aircraft*, Vol. 48, No. 4, 2011, pp. 1245–1253. https://doi.org/10.2514/1.C031248, URL https://doi.org/10.2514/1.C031248.

[21] Rallabhandi, S. K., "Propagation Analysis Using sBOOM for the Third AIAA Sonic Boom Prediction Workshop," *Journal of Aircraft*, Vol. 59, No. 3, 2022, pp. 697–707. https://doi.org/10.2514/1.C036325, URL https://doi.org/10.2514/1.C036325.

[22] Chan, W., *Developments in Strategies and Software Tools for Overset Structured Grid Generation and Connectivity*, 2011. https://doi.org/10.2514/6.2011-3051, URL https://arc.aiaa.org/doi/abs/10.2514/6.2011-3051.

[23] Armijo, L., "Minimization of functions having Lipschitz continuous first partial derivatives," *Pacific Journal of mathematics*, Vol. 16, No. 1, 1966, pp. 1–3.

[24] Nakahashi, K., and Deiwert, G. S., "Three-dimensional adaptive grid method," *AIAA Journal*, Vol. 24, No. 6, 1986, pp. 948–954. https://doi.org/10.2514/3.9369, URL https://doi.org/10.2514/3.9369.

[25] Harvey, A. D., Acharya, S., Lawrence, S. L., and Cheung, S., "Solution-adaptive grid procedure for high-speed parabolic flow solvers," *AIAA Journal*, Vol. 29, No. 8, 1991, pp. 1232–1240.

[26] Venditti, D. A., and Darmofal, D. L., "Adjoint Error Estimation and Grid Adaptation for Functional Outputs: Application to Quasi-One-Dimensional Flow," *Journal of Computational Physics*, Vol. 164, No. 1, 2000, pp. 204–227. https://doi.org/https://doi.org/10.1006/jcph.2000.6600, URL https://www.sciencedirect.com/science/article/pii/S0021999100966002.

[27] Venditti, D. A., and Darmofal, D. L., "Grid Adaptation for Functional Outputs: Application to Two-Dimensional Inviscid Flows," *Journal of Computational Physics*, Vol. 176, No. 1, 2002, pp. 40–69.

[28] Buning, P., and Pulliam, T., *Cartesian Off-Body Grid Adaption for Viscous Time-Accurate Flow Simulations*, 2011. https://doi.org/10.2514/6.2011-3693, URL https://arc.aiaa.org/doi/abs/10.2514/6.2011-3693.

[29] Choudhary, A., Tyson, W. C., and Roy, C. J., "Implementation and Assessment of a Residual-Based r-Adaptation Technique on Structured Meshes," *Journal of Verification, Validation and Uncertainty Quantification*, Vol. 3, No. 4, 2019. https://doi.org/10.1115/1.4043652, URL https://doi.org/10.1115/1.4043652, 041005.